PAPER • **OPEN ACCESS**

Electron dynamics in planar radio frequency magnetron plasmas: I. The mechanism of Hall heating and the μ-mode

To cite this article: Denis Eremin *et al* 2023 *Plasma Sources Sci. Technol.* **32** 045007

OPEN ACCESS
IOP Publishing
Plasma Sources Science and Technology
Plasma Sources Sci. Technol. **32** (2023) 045007 (20pp)
https://doi.org/10.1088/1361-6595/acc481

Electron dynamics in planar radio frequency magnetron plasmas: I. The mechanism of Hall heating and the μ-mode

Denis Eremin[1,*], Dennis Engel[1], Dennis Krüger[1], Sebastian Wilczek[2], Birk Berger[2], Moritz Oberberg[2], Christian Wölfel[3], Andrei Smolyakov[4], Jan Lunze[3], Peter Awakowicz[2], Julian Schulze[2] and Ralf Peter Brinkmann[1]

[1] Institute of Theoretical Electrical Engineering, Ruhr University Bochum, Bochum, Germany
[2] Chair of Applied Electrodynamics and Plasma Technology, Ruhr University Bochum, Bochum, Germany
[3] Institute of Automation and Computer Control, Ruhr University Bochum, Bochum, Germany
[4] Department of Physics and Engineering Physics, University of Saskatchewan, Saskatoon, Canada

E-mail: denis.eremin@rub.de

Received 13 October 2022, revised 3 February 2023
Accepted for publication 15 March 2023
Published 11 April 2023

Abstract

The electron dynamics and the mechanisms of power absorption in radio-frequency (RF) driven, magnetically enhanced capacitively coupled plasmas at low pressure are investigated. The device in focus is a geometrically asymmetric cylindrical magnetron with a radially nonuniform magnetic field in axial direction and an electric field in radial direction. The dynamics is studied analytically using the cold plasma model and a single-particle formalism, and numerically with the inhouse energy and charge conserving particle-in-cell/Monte Carlo collisions code ECCOPIC1S-M. It is found that the dynamics differs significantly from that of an unmagnetized reference discharge. In the magnetized region in front of the powered electrode, an enhanced electric field arises during sheath expansion and a reversed electric field during sheath collapse. Both fields are needed to ensure discharge sustaining electron transport against the confining effect of the magnetic field. The corresponding azimuthal $\mathbf{E} \times \mathbf{B}$-drift can accelerate electrons into the inelastic energy range which gives rise to a new mechanism of RF power dissipation. It is related to the Hall current and is different in nature from Ohmic heating, as which it has been classified in previous literature. The new heating is expected to be dominant in many magnetized capacitively coupled discharges. It is proposed to term it the 'μ-mode' to separate it from other heating modes.

Keywords: RF magnetrons, new electron heating mode, collisionless electron energization, magnetized plasma, Hall heating

(Some figures may appear in colour only in the online journal)

* Author to whom any correspondence should be addressed.

1. Introduction

An externally applied magnetic field allows to sustain gas discharges at lower pressures and at higher plasma densities than otherwise possible [1]. Magnetically enhanced plasmas play a major role in advanced surface processing technologies such as thin film deposition, plasma etching, or ion implantation [2–6]. They are often termed 'partially' or 'weakly' magnetized, referring to the fact that—at typical magnetic flux densities B of up to 100 mT—only electrons are magnetized, while ions are not. (A particle is called magnetized when its gyration radius r_L is smaller than other length scales like the reactor size L, the scale length of the magnetic field l, and the mean free path λ, and its gyration frequency ω_c larger that than other relevant frequencies like the excitation frequency ω_RF or the collision frequency ν [7]). In this study, we focus on radio-frequency (RF) driven magnetrons [8, 9], or, more generally, on magnetically enhanced capacitively coupled plasmas (MECCPs), where a RF voltage drives an electrical current across the magnetic field [10].

In order to optimize and control such discharges, it is crucial to understand how exactly magnetized electrons acquire and utilize their power. The aspect of 'utilization' is obvious: magnetization can confine energetic electrons to an active region which they can leave only by collisional interaction (classical transport) or by scattering at instability-induced fluctuations of the electric field (anomalous transport). This improves utilization of the electron energy. In some discharge configurations such as planar magnetrons, the electron drift orbits are closed within the reactor, so that the effective system size becomes infinite [11].

The processes which enable the electrons to acquire energy are more difficult to address. In a fluid view, electron heating, as the phenomenon is called, requires an electron current $\boldsymbol{j}_\mathrm{e}$ in the direction of the electric field $\boldsymbol{E}$: The power dissipation, i.e. the energy flow from the electromagnetic field to the electrons, is equal to $P_\mathrm{e} = \boldsymbol{j}_\mathrm{e}\cdot\boldsymbol{E}$. The mechanisms underlying the transport of electrons in magnetized plasmas are diverse and notoriously complicated [12, 13]. Equally complicated are the mechanisms of electron heating in MECCPs. Note that the fluid picture itself may be physically insufficient and should be supplemented by kinetic analysis: only those electrons whose kinetic energies are above the inelastic thresholds of chemical reactions can create useful new particles and radiation. Low-energy electrons do not have this chance and merely take part in transport processes. This consideration would motivate to distinguish between electron heating in general and electron energization in particular [14].

To get oriented, it helps to first consider the power absorption in non-magnetized CCPs. Traditionally, Ohmic heating was assumed: The electrical field parallel to the electron flux was taken to arise from Ohmic resistance, i.e. from the need to overcome electron inertia and the momentum loss connected to elastic collisions with the neutral background particles [1]. This process can already be captured within the Drude model. (We use standard notation: m_e is the electron mass, e the electron charge, n_e the electron density, ω_RF the frequency of the applied voltage, and $\nu_\mathrm{e} = v_\mathrm{the}/\lambda_\mathrm{e}$ the electron neutral collision frequency, where λ_e is the mean free path and $v_\mathrm{the} = \sqrt{8T_\mathrm{e}/\pi m_\mathrm{e}}$ the thermal speed; T_e is the electron temperature). In the frequency domain, the plasma conductivity is the complex $\underline{\sigma}_\mathrm{e} = e^2 n_\mathrm{e}/(i\omega_\mathrm{RF} + \nu_\mathrm{e})m_\mathrm{e}$ (denoted as such by an underline). The electron current is $\underline{\boldsymbol{j}}_\mathrm{e} = \underline{\sigma}_\mathrm{e}\underline{\boldsymbol{E}}$, and the phase-averaged dissipated power, understood to be converted into electron thermal energy, reads:

$$\bar{P}_\Omega = \frac{1}{4}\left(\underline{\boldsymbol{j}}_\mathrm{e}\cdot\underline{\boldsymbol{E}}^* + \underline{\boldsymbol{j}}_\mathrm{e}^*\cdot\underline{\boldsymbol{E}}\right) = \frac{e^2 n_\mathrm{e}\nu_\mathrm{e}}{2m_\mathrm{e}\left(\nu_\mathrm{e}^2 + \omega_\mathrm{RF}^2\right)}\underline{\boldsymbol{E}}\cdot\underline{\boldsymbol{E}}^*. \quad (1)$$

Kinetic theory gives insight into the underlying mechanism. Assuming that the electric field is not too strong—$e\lambda_\mathrm{e}|\boldsymbol{E}| \ll T_\mathrm{e}$, so that the energy increment between collisions is small—, Ohmic heating is a diffusion process in energy space. The corresponding diffusion constant is proportional to the square of the effective electric field and, provided that the elastic collision frequency is smaller than the radio frequency, proportional to the pressure p [15, 16]. At low gas pressure, however, the concept of Ohmic heating loses its explanatory power. An alternative mechanism, termed 'stochastic heating', was proposed by Godyak [17, 18]. The modulated plasma sheath, specifically the electron edge, was treated as an oscillating, specularly reflecting 'hard wall'. As a consequence, if an electron of velocity v collides with the edge moving at speed u_s, then the electron velocity after the collision is $2u_\mathrm{s} - v$. Under the assumption that the oscillation of the electron edge and the trajectories of the individual electrons are not correlated—which explains the term 'stochastic heating'—, this process leads, on average, to an increase in kinetic energy. (It is evident that the stated assumption is problematic, and recent treatments seek to avoid it. However, the name stuck). Further investigations have shown that, for typical plasma conditions, stochastic heating cannot really be of a collision-free nature. Rather, it must be of a 'hybrid' type in that it requires an additional dissipative mechanism in the plasma bulk, for example elastic electron-neutral collisions, even if these are only implicitly accounted for [19, 20].

It was also found that not only the moving sheath edge, but also the momentarily quasineutral zone behind it contributes to the power dissipation via the ambipolar field [21, 22]. The concept of 'pressure heating' is based on the assumption that sheath heating is caused by the periodic but temporally asymmetric compression and decompression of the electron fluid near the sheath [21, 23]. Lafleur *et al* [24] argued that stochastic heating and pressure heating stem from the same physical mechanism; they differ only in the spatial region where the electron heating is assumed to occur. For a finite net power absorption, the sheath expansion must not be a 'mirror image' of the collapse, so that the dissipation integral $\oint \boldsymbol{j}_\mathrm{e}\cdot\mathrm{d}\boldsymbol{E}$ is unequal to zero [23, 25].

Additional electron heating mechanisms which can be linked to sheath physics are caused by the action of a reversed electric field during sheath collapse ('field reversal heating') [26–30] and the self-excitation of the plasma series resonance (PSR) through sheath-related nonlinearities in asymmetric

discharges ('nonlinear electron resonance heating' (NERH)) [31–36]. Lastly, it was found that also secondary electrons, predominantly of the ion-induced γ-type, can significantly contribute to the electron heating process and even enable a transition of the discharge into the γ-mode [37, 38]. Of course, all listed processes are simultaneously present and may act in synergy [39].

The literature on the subject shows that all heating mechanisms present in unmagnetized capacitive plasmas can also be seen in their magnetized counterparts, albeit in modified form. An early study by Lieberman, Lichtenberg, and Savas stated that both Ohmic and stochastic heating would be enhanced by a magnetic field, but via different physical mechanisms [40]. The increased Ohmic heating was related to a magnetically modified conductivity tensor. Stochastic heating would increase because magnetized electrons can collide multiple times with the sheath during an expansion phase, at each collision picking up additional energy. Both heating processes were argued to scale positively with the magnetic field strength, so that their ratio was predicted to stay constant. Another early study found increased levels of sheath heating under the resonance condition $\omega = 2\omega_{ce}$ [41]. This effect, which requires unusually small magnetic fields, was revisited in [42, 43], where it acquired a new name 'electron bounce-cyclotron resonance heating'. Later research came to different results. Using experiments, particle-in-cell/Monte Carlo collisions (PIC/MCCs) simulations, or analytical models, references [44–46] claimed that even weak magnetic fields could make Ohmic heating prevail over other heating mechanisms. More recent work has argued similarly [47–49].

Also the other mechanisms were seen in magnetized plasmas. NERH was investigated for different values of the magnetic flux density in RF driven planar magnetron plasmas [50, 51]. Electric field reversal was also observed and connected with the inhibited electron transport due to the magnetic field [10, 52–54]. Influence of ambipolar field heating was seen in [54]. Also secondary electron emission can play a role. Kushner concluded that if the magnetic field is oriented parallel to the electrode, heating by secondary electrons (of the γ-type) is most effective when their gyroradius is comparable to the elastic mean free path [10]. Other research, however, indicated that a presence of secondaries is not always important for discharge sustainment [55].

As stated above, all electron heating mechanisms present in unmagnetized capacitive plasmas are also active in MECCPs, albeit in modified form. But does this also apply vice versa? Can all electron heating processes in MECCPs be understood in terms of their counterparts in unmagnetized CCPs? We do not believe this is the case. Instead, we believe that the dominant heating in MECCPs is 'truly magnetic' but has not been recognized as such. In particular, we believe that the term 'Hall-enhanced Ohmic heating' [49] is a misnomer, and that the underlying phenomenon has little in common with the process of Ohmic heating, provided that term is used in the original sense. We propose to call it 'Hall heating' or, with reference to the role of the magnetic field, the 'μ-mode'. In this study we will outline our arguments and support them with analysis and simulation. Specifically, we will contrast the characteristics of a magnetized discharge with a nominal field strength of $B = 5\,\mathrm{mT}$ with an unmagnetized reference case of the same geometry. (If necessary, we mark the magnetized and unmagnetized case with (M) and (U), respectively).

This publication is the first of three companion papers aimed at improving the understanding of the electron dynamics in magnetized RF discharges operated at low pressures. It emphasizes the kinetic nature of the electron heating in such discharges and demonstrates that the dominant Hall heating is a new mechanism that directly leads to efficient ionization. To focus on the electron transport across the magnetic field lines, we study a deliberately simplified system, namely a long, axisymmetric cylindrical magnetron. The second work [56] computationally studies a planar RF magnetron in realistic geometry with electron motion along and across the magnetic field. Finally, the third publication [57] presents experimental observations obtained in a planar RF magnetron and interprets them with help of the newly gained knowledge about the electron dynamics in such devices.

2. The device under study and its operation regime

Our research focuses on a cylindrical magnetron with pronounced geometrical asymmetry. Figure 1 provides a schematic and defines the reference directions of the currents and voltages. The powered inner electrode E has a radius of $R_E = 1\,\mathrm{cm}$, the grounded outer electrode G a radius of $R_G = 6.5\,\mathrm{cm}$, with $R_C = (R_E + R_G)/2$. The electrode area ratio is $A_E/A_G = 0.154$. Invariance in the axial and azimuthal directions is assumed. The first assumption makes the discharge infinitely long. (For evaluation purposes, we use a nominal height of $H = 10\,\mathrm{cm}$). The second assumption reflects that symmetry breaking plasma instabilities are generally not significant for the rather weak magnetic fields ($B \leqslant 10\,\mathrm{mT}$) considered in this study [58–60]. In the radial direction the magnetic field and the plasma characteristics are nonuniform. The device is operated in argon at a pressure of $p = 0.5\,\mathrm{Pa}$ and a temperature of $T = 300\,\mathrm{K}$. A sinusoidal RF voltage with an amplitude of $\hat{V} = 300\,\mathrm{V}$ and a frequency of $f = 13.56\,\mathrm{MHz}$ is connected via a large blocking capacitor, over which a self bias of $\bar{V}_G = -161\,\mathrm{V}$ drops. (All quantitative information corresponds to the simulation results described in section 7). The sheath before the powered electrode has a phase-averaged thickness of $\bar{s}_E \approx 0.32\,\mathrm{cm}$; it develops a large voltage $\bar{V}_E = 200\,\mathrm{V}$ that accelerates the impacting ions to high energies. This, in turn, yields a high flux of secondary electrons which are also energized in the sheath. Analogous processes at electrode G are less effective, there $\bar{s}_G \approx 0.14\,\mathrm{cm}$ and $\bar{V}_G = 20\,\mathrm{V}$. The magnetic field $\boldsymbol{B} = B_z(r)\boldsymbol{e}_z$ is a 1d model of a planar magnetron field [50, 57, 61, 62]. Following the logic of Trieschmann *et al* [63], we adopt the axial profile of the radial magnetic field component directly above the racetrack from [56], see figure 1. An analytical form is

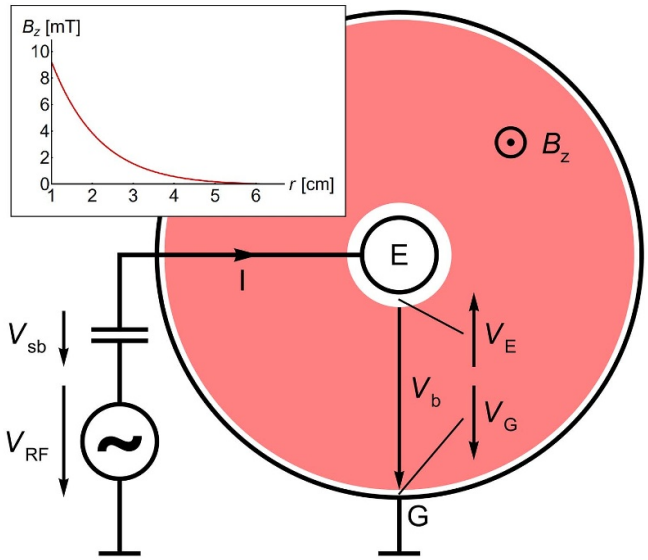

Figure 1. The cylindrical magnetron considered in this study. The discharge is driven by an RF voltage source through a blocking capacitor at the inner electrode, the outer electrode is grounded. The respective radii are $R_E = 1\,\text{cm}$ and $R_G = 6.5\,\text{cm}$. Due to the large geometrical asymmetry, the plasma sheath at the powered electrode is larger than the sheath at the grounded electrode. The magnetic field $B_z(r)$ is axially oriented and non-uniform in the radial direction (see inset). The arrows indicate the sign conventions for the voltages and currents.

as follows, where $B_i = \{-1.46, 21.98, -0.90, 9.92\}\,\text{mT}$ and $\lambda_i = \{35.4, 81.2, 127.3, 173.4\}\,\text{m}^{-1}$:

$$B_z(r) = \sum_{i=1}^{4} B_i \exp(-\lambda_i r). \tag{2}$$

Figure 2 shows the frequency and length scales of the discharge. In the magnetized region, the electron gyro frequency and the plasma frequency are comparable, $\omega_{ce} \approx \omega_{pe} \approx 10^9\,\text{s}^{-1}$, while the RF and the collision rate are smaller, $\omega_{RF} \approx 10^8\,\text{s}^{-1}$ and $\nu_e \approx 10^7\,\text{s}^{-1}$. Likewise, the gyroradius and the Debye length are the smallest scales, $r_L \approx \lambda_D \approx 5 \times 10^{-4}\,\text{m}$, the gradient scale is larger, $l \approx 5 \times 10^{-3}\,\text{m}$; and the mean free path even more, $\lambda_e \approx 5 \times 10^{-2}\,\text{m}$. The electron thermal speed and the $E \times B$ drift speed are similar, $v_{the} \approx v_{E\times B} \approx 10^6\,\text{m}\,\text{s}^{-1}$. The ions are not affected by the magnetic field.

3. Analysis based on the cold plasma model

A first insight into the discharge dynamics is obtained by considering the cold plasma model, also known as the Drude model [1]. We adopt the cylindrical geometry as discussed above. The electron plasma frequency $\omega_{pe}(r)$ and the electron gyro frequency $\omega_{ce}(r)$ depend on r; the elastic electron collision frequency ν_e is constant. The equations of continuity and motion for the charge density $\rho(r,t)$ and for the non-vanishing components $j_r(r,t)$ and $j_\theta(r,t)$ of the electric current density are

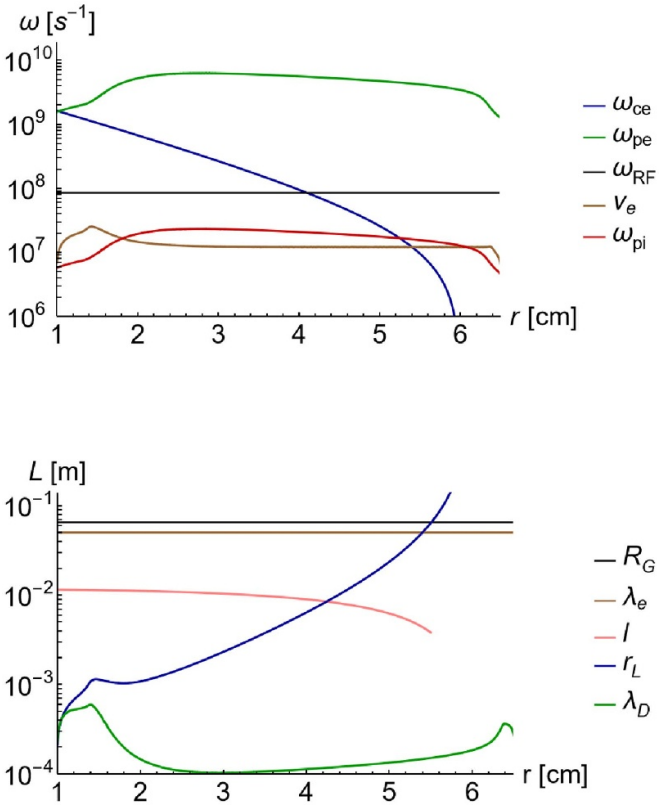

Figure 2. Characteristic frequencies (top) and length scale (bottom) of the cylindrical magnetron. Top: electron gyrofrequency (blue), electron plasma frequency (green), radio frequency (black), electron collision frequency (brown), ion plasma frequency (red). Bottom: chamber radius (black), mean free path (brown), field scale (pink), electron gyroradius (blue), Debye length (green).

$$\frac{\partial \rho}{\partial t} + \frac{1}{r}\frac{\partial}{\partial r}(r j_r) = 0, \tag{3}$$

$$\frac{\partial j_r}{\partial t} = \varepsilon_0 \omega_{pe}^2 E_r - \omega_{ce} j_\theta - \nu_e j_r, \tag{4}$$

$$\frac{\partial j_\theta}{\partial t} = \omega_{ce} j_r - \nu_e j_\theta. \tag{5}$$

The electric field $\boldsymbol{E} = E_r(r,t)\boldsymbol{e}_r$, derived from a potential $\Phi(r,t)$, follows Poisson's equation

$$\varepsilon_0 \frac{1}{r}\frac{\partial}{\partial r}(r E_r) = -\varepsilon_0 \frac{1}{r}\frac{\partial}{\partial r}\left(r\frac{\partial \Phi}{\partial r}\right) = \rho. \tag{6}$$

As a consequence of the equations, the sum of the particle current and the displacement current is divergence-free. This allows to define the current through the discharge as

$$I(t) = 2\pi r\, H\left(j_r + \varepsilon_0 \frac{\partial E_r}{\partial t}\right). \tag{7}$$

If the time-evolution is harmonic with frequency ω (which is in this context not necessarily the applied RF ω_{RF}), the complex

currents $\underline{j}_r$ and $\underline{j}_\theta$ can be expressed as follows. The expressions after the tilde hold in the limiting case $\nu = 0$, $\omega \ll \omega_{ce}$:

$$\underline{j}_r = -\frac{(i\omega + \nu_e)\varepsilon_0\omega_{pe}^2}{\omega^2 - \omega_{ce}^2 - \nu_e^2 - 2i\,\nu_e\omega}\underline{E}_r \sim \frac{i\omega\varepsilon_0\omega_{pe}^2}{\omega_{ce}^2}\underline{E}_r = en_e\frac{i\omega\underline{E}_r}{\omega_{ce}B_z}, \tag{8}$$

$$\underline{j}_\theta = -\frac{\omega_{ce}\varepsilon_0\omega_{pe}^2}{\omega^2 - \omega_{ce}^2 - \nu_e^2 - 2i\,\nu_e\omega}\underline{E}_r \sim \frac{\varepsilon_0\omega_{pe}^2}{\omega_{ce}}\underline{E}_r = en_e\frac{\underline{E}_r}{B_z}. \tag{9}$$

The relation of the discharge current to the electric field can be written as

$$\underline{I} = 2\pi rH\, i\omega\varepsilon_0\varepsilon_p\underline{E}_r, \tag{10}$$

where the relative dielectric constant of the plasma is

$$\varepsilon_p = 1 - \frac{\omega_{pe}^2(\omega - i\,\nu_e)}{\omega\,(\omega^2 - \omega_{ce}^2 - \nu_e^2 - 2i\,\nu_e\omega)} \approx -\frac{\omega_{pe}^2(\omega - i\,\nu_e)}{\omega\,(\omega^2 - \omega_{ce}^2 - \nu_e^2 - 2i\,\nu_e\omega)}. \tag{11}$$

The local resonance condition $\varepsilon_p = 0$ (with full form) leads to a current-free resonance at the upper hybrid frequency $\omega_{uh} = \sqrt{\omega_{pe}^2 + \omega_{ce}^2}$, often termed 'plasma parallel resonance' [36]. If the approximate form of ε_p is used, this fast local phenomenon is excluded and only the slower global behavior remains in the description. Solving (7) for the electric field in terms of the global current I and integrating over the bulk—from $R_E + \bar{s}_E$ to $R_G - \bar{s}_G$—yields the voltage drop over the bulk. Added to this is the capacitive voltage drop over the sheaths. We evaluate the model for the unmagnetized reference case (U) and the magnetized case (M) described in sections 6 and 7 below. For a compact notation, we introduce the inverse capacitances of the two sheaths and the inertia coefficient ('inductance') of the bulk:

$$C_E^{-1} = \int_{R_E}^{R_E+\bar{s}_E}\frac{1}{2\pi r\,H\varepsilon_0}\,\mathrm{d}r = 1.32\times10^{11}\,\mathrm{V\,A s^{-1}\,(U)}\ \text{ or }\ 5.00\times10^{10}\,\mathrm{V\,A s^{-1}\,(M)}, \tag{12}$$

$$C_G^{-1} = \int_{R_G-\bar{s}_G}^{R_G}\frac{1}{2\pi r\,H\varepsilon_0}\,\mathrm{d}r = 1.63\times10^{10}\,\mathrm{V\,A s^{-1}\,(U)}\ \text{ or }\ 3.90\times10^{9}\,\mathrm{V\,A s^{-1}\,(M)}, \tag{13}$$

$$L_B = \int_{R_E+\bar{s}_E}^{R_G+\bar{s}_G}\frac{1}{2\pi r\,H\varepsilon_0\omega_{pe}^2(r)}\,\mathrm{d}r = 1.01\times10^{-7}\,\mathrm{V\,A s^{-1}\,(U)}\ \text{ or }\ 1.66\times10^{-8}\,\mathrm{Vs\,A^{-1}\,(M)}. \tag{14}$$

In the magnetized case there is an additional coefficient, formally an inverse 'capacitance'.

Physically, this capacitive behavior can be understood as follows: the magnetized electrons in the bulk experience $\boldsymbol{E}\times\boldsymbol{B}$ drift, so that their kinetic energy density is $m_e\,(E_r/B_z)^2\,n_e/2$. The energy density of an electric field is $\varepsilon_0\varepsilon_r E_r^2/2$. Formally equating the two yields a 'relative permittivity' of $\varepsilon_r = \omega_{pe}^2/\omega_{ce}^2$. Applying the formula to the series connection of an infinite number of infinitely thin capacitors leads to

$$C_B^{-1} = \int_{R_E+\bar{s}_E}^{R_G+\bar{s}_G}\frac{\omega_{ce}^2(r)}{2\pi r\,H\varepsilon_0\omega_{pe}^2(r)}\,\mathrm{d}r = 0\,\mathrm{V\,A s^{-1}\,(U)}\ \text{ or }\ 9.64\times10^{9}\,\mathrm{V\,A s^{-1}\,(M)}. \tag{15}$$

The impedance of the discharge is then

$$\underline{Z}(\omega) = \frac{C_E^{-1}}{i\omega} + \frac{C_G^{-1}}{i\omega} + (i\omega + \nu_e)L_B + \frac{C_B^{-1}}{(i\omega + \nu_e)}. \tag{16}$$

At the frequency $\omega_{RF} = 2\pi\times13.56\,\mathrm{MHz}$, the overall impedance is dominated by the sheaths and acts as a lossy capacitor, $\underline{Z}(\omega_{RF}) = (1.22 - 1726\,\mathrm{i})\,\mathrm{V\,A^{-1}}$ (U) or $(15.9 - 742\,\mathrm{i})\,\mathrm{V\,A^{-1}}$ (M). This implies that the system response is nearly quasistatic: the discharge state is controlled by the momentary value $V_{RF}(t)$, and the discharge current reflects the derivative $\mathrm{d}V_{RF}/\mathrm{d}t$. Superimposed on this, however, can be an excitation of the PSR. Its frequency is obtained by setting the impedance $\underline{Z}(\omega)$ equal to zero and solving for ω:

$$\omega_{PSR} = \sqrt{\left(C_E^{-1} + C_G^{-1} + C_B^{-1}\right)/L_B} = 1.21\times10^{9}\,\mathrm{s^{-1}\,(U)}\ \text{ or }\ 1.96\times10^{9}\,\mathrm{s^{-1}\,(M)}. \tag{17}$$

In the unmagnetized case, the ratio of the PSR frequency to the RF is about 14; in the magnetized case, the ratio is roughly 23. This shift can be understood in elementary terms by assuming also uniform plasma density and uniform magnetic flux density profiles. Equation (17) gives $\omega_{PSR}(\mathrm{M}) = \sqrt{\omega_{PSR}^2(\mathrm{U}) + \omega_{ce}^2}$ with $\omega_{PSR}(\mathrm{U}) = \sqrt{(\bar{s}_E + \bar{s}_G)/(R_G - R_E)}\,\omega_{pe}$ [64]. The resonances are damped with a rate of $\beta = 6.0\times10^{6}\,\mathrm{s^{-1}}$ (U) or $7.0\times10^{6}\,\mathrm{s^{-1}}$ (M).

4. Single-particle picture

An alternative picture can be established by analyzing the motion of individual electrons. We assume a magnetic field $\boldsymbol{B} = B_z(r)\,\boldsymbol{e}_z$ and an RF modulated electric field $\boldsymbol{E} = E_r(r,t)\,\boldsymbol{e}_r$. For our numerical trajectory example, we take the magnetic field (2) and the electrical field from the simulations below, see figure 18. (The results of this section can thus be compared directly with the simulation outcome). The motion along the magnetic field lines is simple: the coordinate z moves uniformly in time, the velocity v_z is constant:

$$\frac{\mathrm{d}z}{\mathrm{d}t} = v_z, \tag{18}$$

$$\frac{\mathrm{d}v_z}{\mathrm{d}t} = 0. \tag{19}$$

Consequently, also the kinetic energy of the motion along the magnetic field is constant:

$$\frac{\mathrm{d}\epsilon_{\parallel}}{\mathrm{d}t} \equiv \frac{\mathrm{d}\epsilon_z}{\mathrm{d}t} \equiv \frac{\mathrm{d}}{\mathrm{d}t}\left(\frac{1}{2}m_\mathrm{e}v_z^2\right) = 0. \tag{20}$$

The motion in the r-θ-plane is governed by the Lorentz force and the inertial pseudo-forces, with the former typically dominating the latter by an order of magnitude:

$$\frac{\mathrm{d}r}{\mathrm{d}t} = v_r, \tag{21}$$

$$\frac{\mathrm{d}\theta}{\mathrm{d}t} = \frac{v_\theta}{r}, \tag{22}$$

$$\frac{\mathrm{d}v_r}{\mathrm{d}t} = -\frac{e}{m_\mathrm{e}}(E_r + v_\theta B_z) + \frac{v_\theta^2}{r}, \tag{23}$$

$$\frac{\mathrm{d}v_\theta}{\mathrm{d}t} = \frac{e}{m_\mathrm{e}}v_r B_z - \frac{v_r v_\theta}{r}. \tag{24}$$

The kinetic energy in the r–θ-plane is modulated by the power influx from the electric field. As expected, the Lorentz force and the inertial force do not contribute:

$$\frac{\mathrm{d}\epsilon_\perp}{\mathrm{d}t} \equiv \frac{\mathrm{d}}{\mathrm{d}t}(\epsilon_r + \epsilon_\theta) \equiv \frac{\mathrm{d}}{\mathrm{d}t}\left(\frac{1}{2}m_\mathrm{e}v_r^2 + \frac{1}{2}m_\mathrm{e}v_\theta^2\right) = -ev_rE_r. \tag{25}$$

A numerical integration of the cross-sectional equations of motion can easily be carried out. For a medium-energy particle in the strongly magnetized zone, figure 3 displays the trajectory in the cross-sectional r–θ-plane over a single RF period and over a stretch of 25 RF periods. It clearly shows a superposition of gyromotion and drift. Figure 4 displays the evolution of the coordinates $r(t)$ and $\theta(t)$ and the velocities $v_r(t)$ and $v_\theta(t)$ over two RF periods, respectively. Figure 5 shows the corresponding kinetic energies.

It is instructive to compare the numerically calculated trajectories above with approximate solutions constructed by means of perturbation analysis. We apply a technique based on a series expansion in the ratio of the gyroradius to the discharge scale, $\eta = r_\mathrm{L}/|r - R_\mathrm{E}| \approx 0.1$. For a qualitative picture, it suffices to evaluate the power series up to the leading order in η. (appendix provides more mathematical details and formulates also higher order terms.) We start by noting that there is, due to the cylindrical symmetry, a strict constant of motion, the canonical momentum $p_\theta = rm_\mathrm{e}v_\theta - reA_\theta(r)$, where A_θ is the θ-component of the magnetic vector potential $\mathbf{A}$. It can be used to define the temporally constant reference radius $\hat{r}$ of an electron trajectory via the relation $p_\theta \stackrel{!}{=} -\hat{r}eA_\theta(\hat{r})$. In the numerical example, $\hat{r} = 16.1\,\mathrm{mm}$. We use the circumflex also to denote the constant magnetic flux density $\hat{B} = B_z(\hat{r}) = 5.4\,\mathrm{mT}$ at the reference radius $\hat{r}$. The corresponding gyrofrequency is $\hat{\Omega} = e\hat{B}/m_\mathrm{e} = 9.5 \times 10^8\,\mathrm{s}^{-1}$. The temporally varying electric field strength at the reference point is termed $\hat{E}(t) = E_r(\hat{r}, t)$; the corresponding drift speed is $\hat{v}_{E\times B}(t) = \hat{E}(t)/\hat{B}$. An approximate solution of the equations

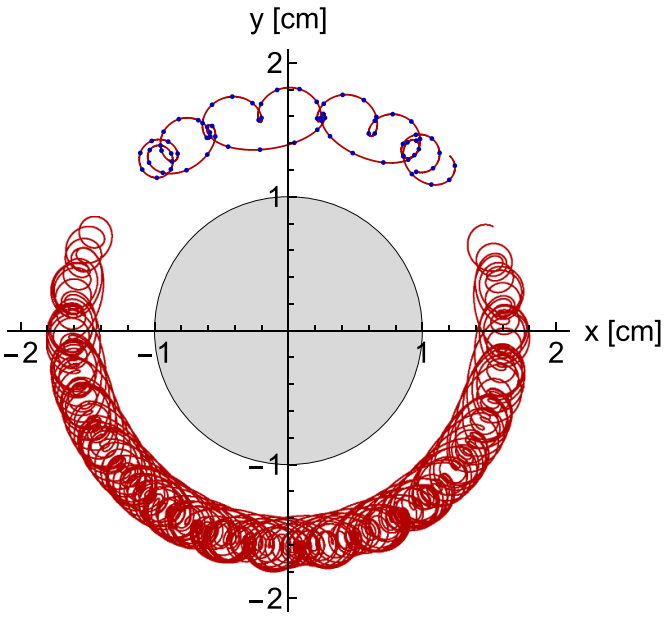

Figure 3. Trajectory of a magnetized electron in the cross-sectional plane, showing the superposition of small scale gyration and large scale drift. Top part: trajectory recorded over one RF period; the blue dots have 1 ns separation. Bottom part: trajectory followed over 25 RF periods.

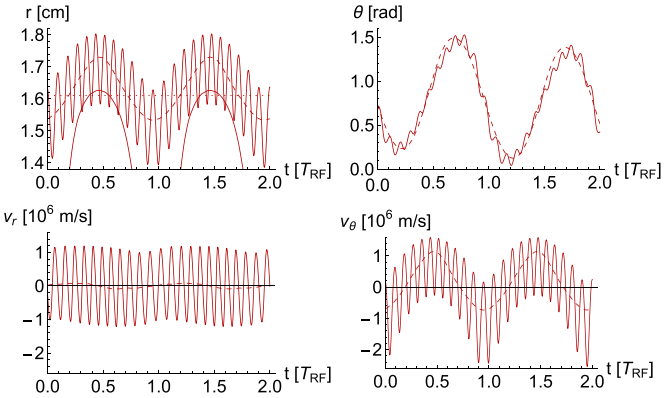

Figure 4. Radial coordinate $r(t)$, azimuth $\theta(t)$, radial velocity $v_r(t)$, and azimuthal velocity $v_\theta(t)$ of the sample trajectory followed over two RF periods. Solid: particle coordinates and velocities. Dashed: coordinates and velocities of the guiding center. Dotted: reference radius $\hat{r}$.

of motion can then be expressed as follows. Note the correspondence of (28) and (29) with (8) and (9) under the assumptions $\nu_\mathrm{e} \to 0$, $\omega \ll \omega_\mathrm{ce}$, and $\hat{\rho} \to 0$:

$$r = \hat{r} - \frac{\hat{v}_{E\times B}}{\hat{\Omega}} + \hat{\rho}\cos\left(\hat{\Omega}t + \hat{\phi}\right), \tag{26}$$

$$\theta = \hat{\theta} + \frac{\hat{\rho}}{\hat{r}}\sin\left(\hat{\Omega}t + \hat{\phi}\right), \tag{27}$$

$$v_r = -\frac{1}{\hat{\Omega}}\frac{\mathrm{d}\hat{v}_{E\times B}}{\mathrm{d}t} - \hat{\Omega}\hat{\rho}\sin\left(\hat{\Omega}t + \hat{\phi}\right), \tag{28}$$

$$v_\theta = -\hat{v}_{E\times B}(t) + \hat{\Omega}\hat{\rho}\cos\left(\hat{\Omega}t + \hat{\phi}\right). \tag{29}$$

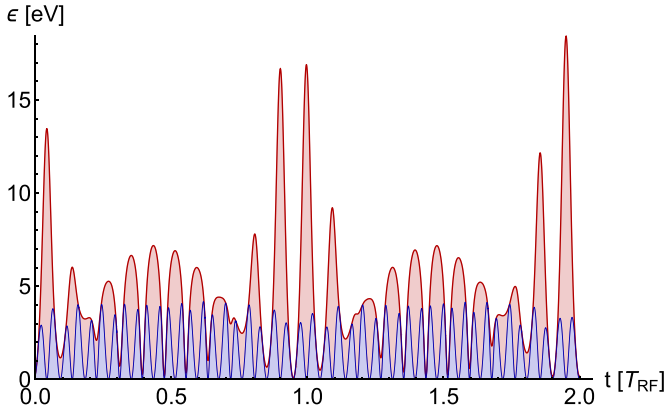

Figure 5. Kinetic particle energy in radial direction (blue) and in azimuthal direction (red) of the sample trajectory over two RF periods. The second curve shows constructive and destructive interference of gyro motion and drift.

The gyroradius $\hat{\rho}$ is an adiabatic constant, i.e. independent of time, while the gyrophase offset $\hat{\phi}$ and the azimuth offset $\hat{\theta}$ exhibit a slow evolution. In the next order approximation, this is described as follows, with the prime indicating the derivative with respect to $\hat{r}$:

$$\frac{\mathrm{d}\hat{\phi}}{\mathrm{d}t} = \frac{3}{2}\left(\frac{1}{\hat{r}} - \frac{\hat{B}'}{\hat{B}}\right)\hat{v}_{E\times B} + \frac{\hat{E}'}{2B}, \tag{30}$$

$$\frac{\mathrm{d}\hat{\theta}}{\mathrm{d}t} = -\frac{1}{\hat{r}}\hat{v}_{E\times B}. \tag{31}$$

The kinetic energy of the electron can be calculated as

$$\begin{aligned}\epsilon \approx{}& \frac{1}{2}m_\mathrm{e}\hat{\Omega}^2\hat{\rho}^2 + \frac{1}{2}m_\mathrm{e}\left(\hat{v}_{E\times B}(t)^2 + \frac{1}{\hat{\Omega}^2}\left(\frac{\mathrm{d}\hat{v}_{E\times B}}{\mathrm{d}t}\right)^2\right)\\ &+ m_\mathrm{e}\hat{\Omega}\hat{\rho}\left(-\cos\left(\hat{\Omega}t+\hat{\phi}\right)\hat{v}_{E\times B}(t)\right.\\ &\left.+\sin\left(\hat{\Omega}t+\hat{\phi}\right)\frac{1}{\hat{\Omega}}\frac{\mathrm{d}\hat{v}_{E\times B}}{\mathrm{d}t}\right) + \frac{1}{2}m_\mathrm{e}v_z^2.\end{aligned} \tag{32}$$

Obviously, the electron dynamics can be described as the superposition of a large-scale drift of the guiding center—first terms in (26)–(29)— and a small-scale gyromotion (last terms). The guiding center trajectories have a banana-like shape, which can be explained physically: the force $\boldsymbol{F} = -e\hat{E}\boldsymbol{e}_r$ perpendicular to $\boldsymbol{B}$ modulates the energy of the gyrating electron; it grows when the electron moves in the direction of $\boldsymbol{F}$ and decreases when it moves otherwise. The net effect is a drift $\boldsymbol{v}_\mathrm{d} = -\hat{v}_{E\times B}(t)\boldsymbol{e}_\theta$. The resulting shift in the azimuthal position $r\Delta\theta$ is of the order of $v_{E\times B}/\omega_\mathrm{RF}$. In contrast, the motion in the radial direction is of second order: Because the drift $\boldsymbol{v}_\mathrm{d}$ is RF modulated, it causes an acceleration that acts as a pseudo-force. The corresponding drift is known as the polarization drift [1], it has a phase shift of 90° and is an order of magnitude smaller than the $\mathbf{E}\times\mathbf{B}$ drift. The corresponding shift $\Delta\boldsymbol{r}_\mathrm{p}$ in the radial position is proportional to the electric field:

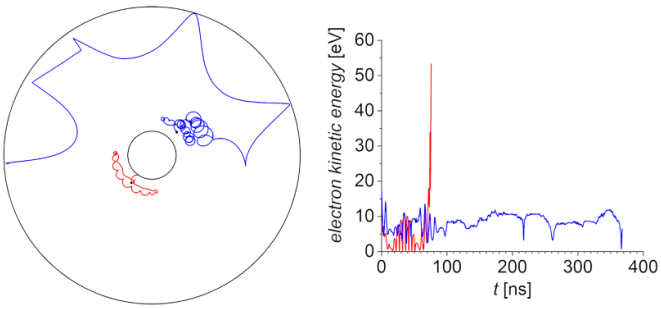

Figure 6. Orbits (left) and kinetic energies (right) of two typical electrons with a similar initial radial location but different initial velocities (see description in the text).

$$\boldsymbol{v}_\mathrm{p} = -m_e\frac{\mathrm{d}\hat{v}_{E\times B}}{\mathrm{d}t}\boldsymbol{e}_\theta \times \frac{\hat{\boldsymbol{B}}}{e\hat{B}^2} = -\frac{1}{\hat{\Omega}}\frac{\mathrm{d}\hat{v}_{E\times B}}{\mathrm{d}t}\boldsymbol{e}_r, \tag{33}$$

$$\Delta\boldsymbol{r}_\mathrm{p} = -\frac{\hat{v}_{E\times B}}{\hat{\Omega}}\boldsymbol{e}_r = -\frac{m_\mathrm{e}\hat{E}}{e\hat{B}^2}\boldsymbol{e}_r. \tag{34}$$

The ratio $\Delta r_\mathrm{p}/r\Delta\theta$ thus scales as $\omega_\mathrm{RF}/\omega_\mathrm{ce} \ll 1$. The banana shape results from the curvature of the azimuthal coordinate lines. The trajectories somewhat resemble the banana-shaped trajectories of the guiding center of trapped particles in tokamaks, although the underlying drift mechanisms are of a different nature [65]. Note that the azimuthal drift velocity and the gyro speed are comparable. The azimuthal kinetic energy ε_r therefore shows destructive and constructive interference; values of nearly 20 eV can be reached, see figure 5.

The approximate solution gives only a qualitative picture. Due to the strong non-uniformity of particularly the electric field at the sheath edge, finite Larmor radius effects play a role. In addition, the motion is strongly influenced by collisions. Figure 6 (left) shows the orbits of two electrons taken from the self-consistent simulation described in section 7 below. Both electrons start near the electrode (marked by black circles) during sheath collapse. The first electron (red) is initially trapped by the magnetic field. It experiences a modulated electric field, which is positive from $t = 0$ ns to $t = 15$ ns, negative from $t = 15$ ns to $t = 57$ ns, and then positive again. The corresponding azimuthal $\boldsymbol{E}\times\boldsymbol{B}$-drift results in a banana-like trajectory of the guiding center, the width of which is determined by the polarization drift. Figure 6 (right) shows that the kinetic energy is also modulated. At $t = 73$ ns and $t = 74$ ns, the electron undergoes elastic collisions which change its orbit and cause it to go to the electrode during the next phase. The other electron (blue) also remains initially trapped close to the electrode, despite collisions at $t = 30$ ns and $t = 70$ ns. Between the elastic collisions, it experiences a strong electric field of changing polarity and changes its energy accordingly. A final collision at $t = 100$ ns scatters the particle near the grounded electrode where the magnetic field is weak. There it follows an orbit with a very large gyroradius and is repeatedly reflected by the potential of the grounded sheath.

5. Kinetic description and velocity moments

For a complete picture of the processes in the discharge, the dynamics of the particles (including collisions and wall interactions) must be coupled to the evolution of the fields. In the low pressure regime of magnetrons, kinetic and non-local phenomena are expected, and a kinetic approach is to be adopted. The particle sector is described by a collection of Boltzmann equations for the distribution functions $f_s = f_s(r, v_r, v_\theta, v_z, t)$, with $s = 1 \ldots N_s$. (Our specific calculations use $s \in \{\mathrm{e}, \mathrm{i}\}$.) For the streaming term on the left, the equations of motion (18) are used, while the term on the right describes the action of collisions:

$$\frac{\partial f_s}{\partial t} + v_r \frac{\partial f_s}{\partial r} + \left(\frac{q_s}{m_s} \left(E_r + v_\theta B_z \right) + \frac{v_\theta^2}{r} \right) \frac{\partial f_s}{\partial v_r} - \left(\frac{q_s}{m_s} v_r B_z + \frac{v_\theta v_r}{r} \right) \frac{\partial f_s}{\partial v_\theta} = C(f_s). \tag{35}$$

Because of the small dimensions of the discharge and the relatively small electron density, the electrostatic approximation can be adopted. The radial electric field E_r is the gradient of the electrostatic potential, $E_r = -\partial\Phi/\partial r$, and Poisson's equation can be written as

$$-\varepsilon_0 \frac{1}{r} \frac{\partial}{\partial r} r \frac{\partial \Phi}{\partial r} = \sum_{s=1}^{N_s} q_s \int f_s \, \mathrm{d}v_r \, \mathrm{d}v_\theta \, \mathrm{d}v_z. \tag{36}$$

A direct solution of these equations with current computational resources is cumbersome. We thus employ ECCOPIC1S-M, a specialized member of our own Energy- and Charge-COnserving PIC (ECCOPIC) suite of GPU-parallelized energy and charge conserving PIC/MCCs codes [66]. ECCOPIC1S-M is an electrostatic 1d3v code for magnetized low pressure discharges in Cartesian, cylindrical, or spherical geometry. It contains several innovations over standard PIC/MCC. The particle positions and potential values are found self-consistently during a time step, using the Crank–Nicolson method inherent to energy-conserving PIC/MCC schemes [67]. The algorithm relaxes the criterion for the onset of the finite grid instability which causes numerical heating in conventional PIC/MCC if the cell size is greater than the Debye length [68]. The accuracy of the orbit integration is controlled by an adaptive sub-stepping technique. An external network with voltage source and blocking capacitor is fully integrated. The collisions are evaluated with the null collision method [69] modified for GPUs [70]; the cross sections are adopted from Phelps [71, 72]. As the plasma density is low, Coulomb collisions are neglected. The ion-induced secondary electron emission coefficient was assumed to be $\gamma = 0.1$ and the sticking coefficient $s = 1$. For details on the implemented algorithms, see [66, 67, 73], for verification of the code family ECCOPIC and benchmarking, see [74–76].

The primary results of a PIC/MCC run are the electric potential values on the grid and the particle positions as functions of time. Single particle trajectories can be recorded as well. More insight into the dynamics can be obtained by reconstructing the velocity moments of the phase-space distribution function f. Defined abstractly as integrals over velocity space, they are realized in the simulation code as sums over all particles in the respective grid cells. To reduce noise, an average is taken over 1000 RF periods after convergence has been reached. Focusing on the electrons and suppressing the index e, we list the electron density

$$n(r,t) = \int f(r, v_r, v_\theta, v_z, t) \, \mathrm{d}^3 v, \tag{37}$$

the mean electron velocities in the directions r and θ,

$$u_r(r,t) = \frac{1}{n} \int v_r f(r, v_r, v_\theta, v_z, t) \, \mathrm{d}^3 v, \tag{38}$$

$$u_\theta(r,t) = \frac{1}{n} \int v_\theta f(r, v_r, v_\theta, v_z, t) \, \mathrm{d}^3 v, \tag{39}$$

and the non-vanishing elements of the pressure tensor,

$$p_{rr}(r,t) = \int m(v_r - u_r)(v_r - u_r) f(r, v_r, v_\theta, v_z, t) \, \mathrm{d}^3 v, \tag{40}$$

$$p_{r\theta}(r,t) = \int m(v_r - u_r)(v_\theta - u_\theta) f(r, v_r, v_\theta, v_z, t) \, \mathrm{d}^3 v, \tag{41}$$

$$p_{\theta\theta}(r,t) = \int m(v_\theta - u_\theta)(v_\theta - u_\theta) f(r, v_r, v_\theta, v_z, t) \, \mathrm{d}^3 v, \tag{42}$$

$$p_{zz}(r,t) = \int m v_z v_z f(r, v_r, v_\theta, v_z, t) \, \mathrm{d}^3 v. \tag{43}$$

Furthermore, we define the following moments of the collision integral,

$$S = \int C(f_s) \, \mathrm{d}^3 v, \tag{44}$$

$$F_r = \int m v_r \, C(f_s) \, \mathrm{d}^3 v, \tag{45}$$

$$F_\theta = \int m v_\theta \, C(f_s) \, \mathrm{d}^3 v. \tag{46}$$

Multiplying the kinetic equation with 1, mv_r and mv_θ and integrating over velocity space yields the particle balance and the momentum balances in the directions of r and θ:

$$\frac{\partial n}{\partial t} + \frac{1}{r} \frac{\partial}{\partial r} \left(r n u_r \right) = S, \tag{47}$$

$$\frac{\partial}{\partial t} \left(m n u_r \right) + \frac{1}{r} \frac{\partial}{\partial r} \left(r \left(m n u_r^2 + p_{rr} \right) \right) - \frac{1}{r} \left(p_{\theta\theta} + m n u_\theta^2 \right) = -e n \left(E_r + u_\theta B_z \right) + F_r, \tag{48}$$

$$\frac{\partial}{\partial t} \left(m n u_\theta \right) + \frac{1}{r^2} \frac{\partial}{\partial r} \left(r^2 \left(m n u_r u_\theta + p_{r\theta} \right) \right) = e n u_r B_z + F_\theta. \tag{49}$$

6. PIC/MCC results: reference case without magnetic field

For reference, let us first consider the simpler unmagnetized case. It follows the logic of all RF-driven capacitive discharges: The plasma self-organizes into the quasineutral bulk and two electron-depleted sheaths in front of the driven and grounded electrodes, respectively. Figure 7 shows the phase-averaged densities of the electrons $\bar{n}_e(r)$ and the ions $\bar{n}_i(r)$ and the electron densities $n_e(r,t)$ at $t=0$ and $t=T_{RF}/2$. The peak density is $n=1.5\times10^{15}\,\mathrm{m}^{-3}$. The electrons can follow the electric field, their plasma frequency $\omega_{pe}=2.2\times10^{9}\,\mathrm{s}^{-1}$ (center) or $\omega_{pe}=6.5\times10^{8}\,\mathrm{s}^{-1}$ (electrode sheath) is larger than the RF $\omega_{RF}=8.5\times10^{7}\,\mathrm{s}^{-1}$. The ions, in contrast, are almost unmodulated and react only on the phase-averaged field; their plasma frequency is $\omega_{pi}=8.0\times10^{6}\,\mathrm{s}^{-1}$ (center) or $\omega_{pi}=2.4\times10^{6}\,\mathrm{s}^{-1}$ (electrode sheath). Figure 8 shows the applied voltage, the discharge and sheaths voltages, and the bias voltage. Figure 9 provides a spatio-temporal map of the electric field $E_r(r,t)$. The electric current $I(t)$ through the discharge (figure 10) is spatially constant, it is the sum of the (small) ion current, the electron current, and the displacement current. Figure 11 shows spatio-temporally resolved maps of the components of this current. The factor $2\pi r$ reflects the cylindrical symmetry of the device, H is its nominal height:

$$I(t)=2\pi rHj(r,t)=2\pi r\,H\left(en_iu_i-en_eu_e+\varepsilon_0\frac{\partial E_r}{\partial t}\right). \quad (50)$$

Due to the cylindrical device geometry, the current densities at the driven and the grounded electrode scale like $j_E:j_G=R_G:R_E=6.5:1$. This makes the discharge strongly asymmetric; the inner sheath is much wider ($\bar{s}_E=1.1\,\mathrm{cm}$) than the grounded outer sheath ($\bar{s}_G=0.56\,\mathrm{cm}$). To understand the electric behavior of the discharge, it is useful to consult a simplified model which analyzes the evolution of the charges in the driven and grounded sheath,

$$Q_E=H\int_{R_E}^{R_C}e(n_i-n_e)\,2\pi r\,\mathrm{d}r, \quad (51)$$

$$Q_G=H\int_{R_C}^{R_G}e(n_i-n_e)\,2\pi r\,\mathrm{d}r. \quad (52)$$

The RF current modulates the charges of the two sheaths. Neglecting small terms related to charge carrier losses to the electrodes, we write as follows, where the charge quantity $\tilde{Q}(t)$ is the phase-average-free integral of $-I(t)$, see figure 12:

$$\frac{\mathrm{d}Q_E}{\mathrm{d}t}=-\frac{\mathrm{d}Q_G}{\mathrm{d}t}=-I(t)=\frac{\mathrm{d}\tilde{Q}}{\mathrm{d}t}. \quad (53)$$

The voltage drop over the discharge $V(t)$ is equal to the sum of the applied RF voltage $V_{RF}(t)$ and the nearly constant self-bias $V_{sb}=-224\,\mathrm{V}$. Assuming that the sheath voltages V_E and V_G are functions of Q_E and Q_G, respectively (figure 13), and neglecting all other electric fields, a voltage balance can be formulated. Here, the offset charges $\bar{Q}_E$, $\bar{Q}_G$ and the self bias V_{sb}

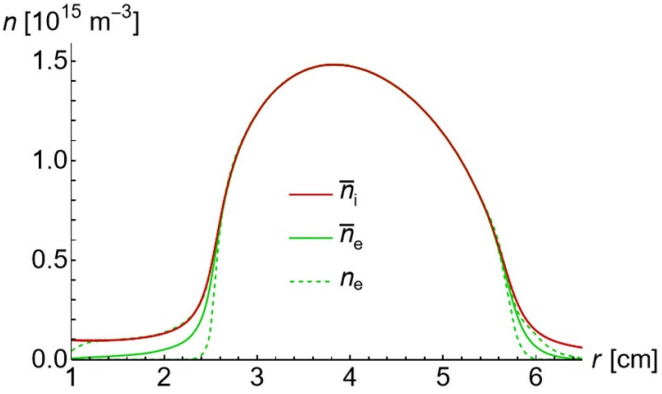

Figure 7. RF period-averaged ion density $\bar{n}_i(r)$ (solid red) and electron density $\bar{n}_e(r)$ (solid green) of the unmagnetized reference discharge. The dashed green lines denote electron densities $n_e(r,t)$ at the sheath minimum (t = 0) and maximum (t = TRF/2), respectively.

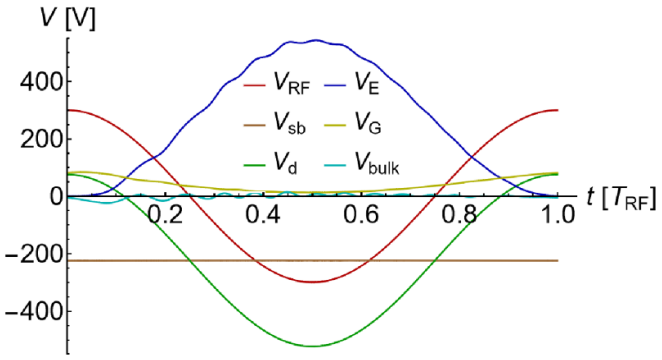

Figure 8. Phase-resolved curves of the applied source voltage $V_{RF}(t)$, the self bias voltage $V_{sb}(t)$, the total discharge voltage $V_d(t)$, the sheath voltages $V_E(t)$ and $V_G(t)$, and the voltage drop $V_{bulk}(t)$ over the plasma bulk for the unmagnetized reference case.

are constants which self-adjust so that the floating condition holds:

$$-V_E\left(\bar{Q}_E+\tilde{Q}(t)\right)+V_G\left(\bar{Q}_G-\tilde{Q}(t)\right)-V_{sb}=V_{RF}\cos(\omega t). \quad (54)$$

This quasistatic model explains much of the electrical behavior: the sheath voltages and the bias voltage are determined by the voltage $V_{RF}(t)$. The periodic charging and discharging of the sheaths gives rise to the discharge current $I(t)$. However, the model over-idealizes: its predicts that the charges and voltages are *exact* functions of the RF voltage $V_{RF}(t)$, and that the discharge current $I(t)$, being a derivative of $\tilde{Q}(t)$, has an *exact* 90° phase shift. This would imply zero net heating. (See the appendix of [25] for details on this argument.)

In reality, and in the results of the PIC/MCC simulation, the current–voltage phase angle is not exactly 90° but very close to it,

$$\cos\varphi=\frac{1}{T}\int_0^T IV\,\mathrm{d}t\Big/\sqrt{\frac{1}{T}\int_0^T I^2\,\mathrm{d}t\,\frac{1}{T}\int_0^T V^2\,\mathrm{d}t}$$
$$=0.0439=\cos 87.5^\circ, \quad (55)$$

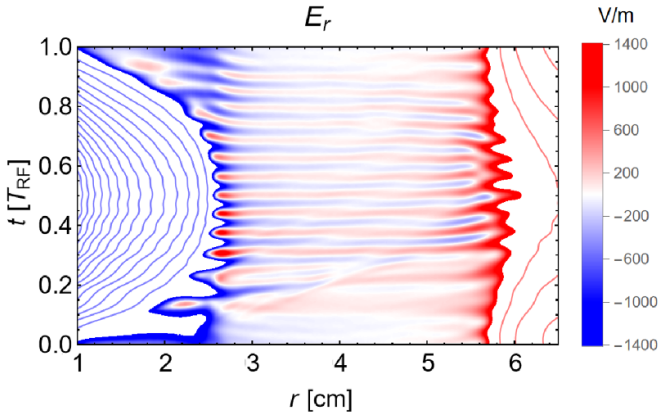

Figure 9. Spatio-temporally resolved electric field $E_r(r,t)$ for the unmagnetized reference discharge. The color shading is scaled to resolve the weak fields in the plasma; the additional contour lines have a separation of $\Delta E = 5000\,\mathrm{V\,m^{-1}}$. The plasma-sheath transition is indicated by the black contours $n_e/n_i = 0.1, 0.5, 0.9$ (from inside to outside) which will be used also in other figures.

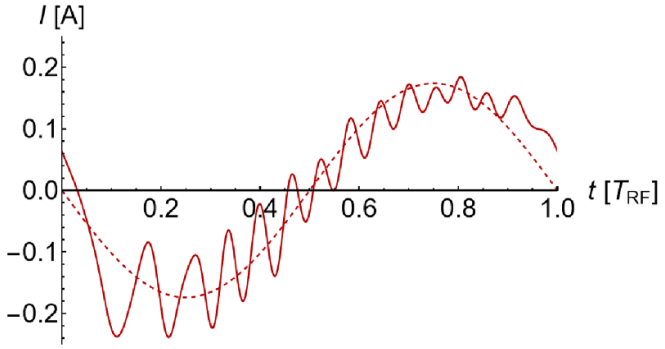

Figure 10. Discharge current $I(t)$ of the unmagnetized case (solid) in comparison with the discharge current of the corresponding Drude model (dashed).

and the phase-averaged dissipation is not zero but

$$\bar{P} = \frac{1}{T}\int_0^T IV\,\mathrm{d}t = 1.22\,\mathrm{W}. \tag{56}$$

Responsible for the non-vanishing heating are, in fact, the small 'other electric fields' that were neglected in the voltage balance (54). These small fields are needed to locally drive the current density $j(r,t)$ which corresponds to the globally determined discharge current $I(t)$. (They are also not well represented in the cold plasma model whose predictions of $\phi = 89.96°$ for the phase angle and $\bar{P} = 0.018\,\mathrm{W}$ for the Ohmically dissipated power are unrealistic. However, the cold plasma model explains well the current oscillations related to the PSR; the predicted value of $\omega_{PSR} = 1.29 \times 10^9\,\mathrm{s^{-1}}$ agrees with the outcome of the simulations.) In the vicinity of the sheaths, where the local plasma frequency $\omega_{pe}(r)$ is close to ω_{PSR}, also Langmuir oscillations occur [77]; see the phase-resolved maps of the electric field $E_r(r,t)$, the particle current $j_r(r,t)$, and the displacement current $j_d(r,t)$. The hallmark of Langmuir oscillations is a 180° degree phase shift between j_r and j_d.

Of the power $\bar{P} = 1.22\,\mathrm{W}$ provided by the RF source, $\bar{P}_i = 0.91\,\mathrm{W}$ are absorbed by the ions and $\bar{P}_e = 0.31\,\mathrm{W}$ by the electrons. The energy transfer to the ions takes place in the sheaths and can be described in terms of the period-averaged field $\bar{E}_r$. The energy exchange between the electric field and the electrons, however, is a complex spatio-temporal phenomenon, involving both the RF excitation and the self-excited PSR. Insight is gained from a velocity moment analysis of the kinetic equation [25, 78]. We solve the momentum balance (48) for the electric field which then can be separated into the inertia field, the pressure field, and the collisional field:

$$\begin{aligned} E_r &= -\frac{1}{en}\left(\frac{\partial}{\partial t}(mnu_r) + \frac{1}{r}\frac{\partial}{\partial r}\left(rmnu_r^2\right) - \frac{mnu_\theta^2}{r}\right) \\ &\quad - \frac{1}{ren}\left(\frac{\partial}{\partial r}(rp_{rr}) - p_{\theta\theta}\right) + \frac{\dot{\pi}_r}{en} \\ &\equiv E_{ir} + E_{pr} + E_{cr}. \end{aligned} \tag{57}$$

Multiplying by $rj_r = -renu_r$, we establish the mechanical energy balance and obtain a split of the radially weighted electron power dissipation rP_{er}, see figure 14,

$$\begin{aligned} rP_{er} = rj_eE_r &= rmu_r\left(\frac{\partial}{\partial t}(nu_r) + \frac{1}{r}\frac{\partial}{\partial r}\left(rnu_r^2\right) - \frac{nu_\theta u_\theta}{r}\right) \\ &\quad + u_r\left(\frac{\partial}{\partial r}(rp_{rr}) - r\frac{p_{\theta\theta}}{r}\right) - ru_r\dot{\pi}_r \\ &\equiv rP_{ir} + rP_{pr} + rP_{cr}. \end{aligned} \tag{58}$$

There is almost no electron heating in the plasma bulk; virtually all RF power is absorbed in the temporarily quasineutral sections of the sheaths. All the heating processes discussed in section 1 are present, but are of different importance. 'Classical' Ohmic heating is weak: the collisional term rP_c contributes only 25% to rP_e, not surprising at the small gas pressure of only $p = 0.5\,\mathrm{Pa}$. The inertia term rP_i can be momentarily large but is small on average. (This reflects that inertia forces are often non-dissipative: electrons accelerated during one half phase of PSR oscillations can be decelerated in the other and feed their energy back.) The main contribution is thus embodied in the pressure term P_{pr}.

A kinetic analysis can refine this picture. Immediately after sheath collapse, in the interval $t = 0.02\,T_{RF}$ to $t = 0.14\,T_{RF}$, the electrode sheath expands with a speed of $u_s \approx 2 \times 10^6\,\mathrm{m\,s^{-1}}$, this high speed arises from a synergy of the RF excitation and the PSR oscillation excited at the moment of sheath collapse [31]. The fast moving sheath reflects the incoming electrons according to $v \to 2u_s - v$. A group of energetic electrons forms, which, further accelerated by the ambipolar field of the presheath, propagate beam-like towards the grounded electrode. This can be seen in figure 15 which displays the radially weighted, spatio-temporally resolved profile of the ionization term. Before the grounded electrode, the energetic beam is stopped by the ambipolar field and by the retreating sheath, giving rise to a negative power density.

However, before reaching that region, some of them have lost their directed energy already by collisions in the bulk, so that even if the rest is fully decelerated by the opposite sheath,

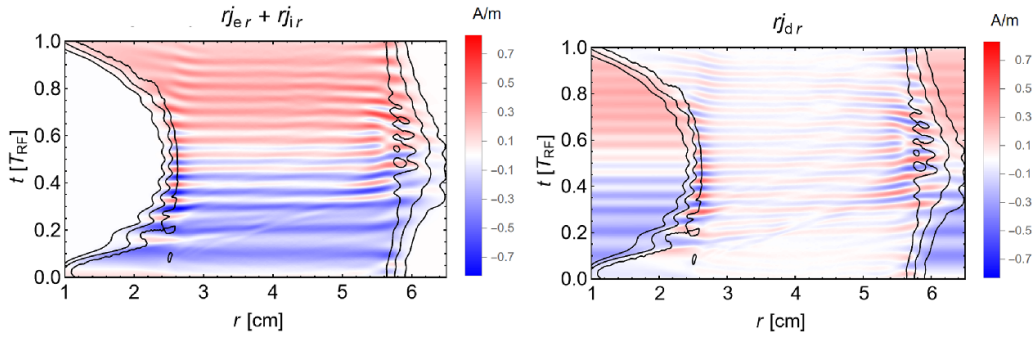

Figure 11. r-weighted particle current $rj_r(r,t)$ (top) and displacement current $rj_{dr}(r,t)$ (bottom) of the unmagnetized reference discharge. Note that the sum of the two is radially invariant.

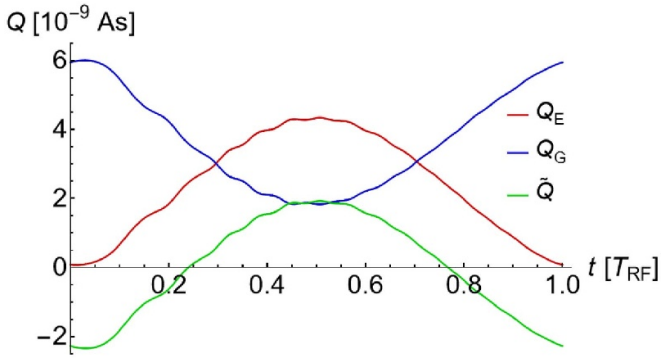

Figure 12. Charges of the electrode sheath $Q_E(t)$ and the ground sheath $Q_G(t)$ together with the average-free integral $\tilde{Q}(t)$ of the current $I(t)$ for the unmagnetized reference case.

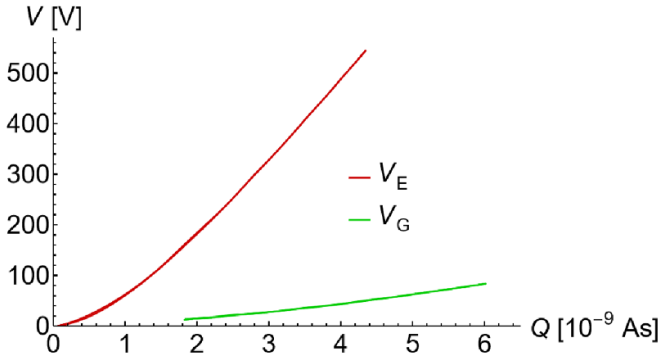

Figure 13. Parametric plot of the electrode sheath voltage $V_E(t)$ and the ground sheath voltage $V_E(t)$ versus the sheath charges $Q(t)$ for the unmagnetized reference case.

the period-averaged energy transfer rate is positive. In the second half of the RF period, the sheaths switch roles, but with less effect on the heating process, since the sheath before the grounded electrode is less strongly modulated. Another source of temporal asymmetry can be attributed to different electron temperatures during sheath expansion and collapse, also resulting in a positive period-averaged power absorption [22, 25]. Heating is therefore substantial in two situations: when there is a violent acceleration of a significant fraction of particles at the

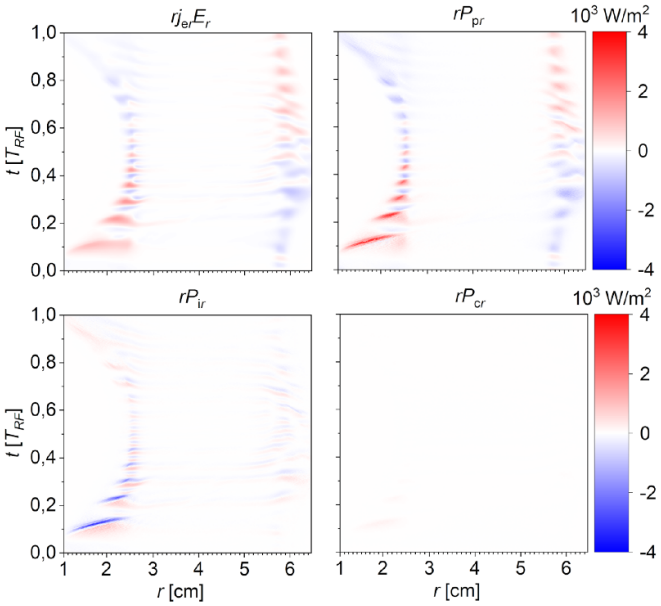

Figure 14. The radially weighted spatio-temporally resolved total power transfer rP_{er} from the electric field to electrons in the radial direction and its constituents (P_{pr}, P_{cr}, P_{ir}) from equation (58) for the unmagnetized reference discharge.

sheath edge, or at the sheath-presheath boundary where a significant temporally asymmetric ambipolar field is present [22].

7. Case with magnetic field

We now turn to the more complex magnetized case. (Figure 1 gives a true-to-scale schematic.) Also this discharge self-organizes into a quasineutral bulk and two electron-depleted sheaths in front of the driven and grounded electrodes, respectively. Its plasma density, however, is 7.5 times higher, the peak density is $n_{max} = 1.24 \times 10^{16}\,\mathrm{m}^{-1}$. The sheaths are thinner by nearly a factor of four, $\bar{s}_E = 0.32\,\mathrm{cm}$ and $\bar{s}_G = 0.14\,\mathrm{cm}$. Figure 16 shows the phase-averaged densities $\bar{n}_i(r)$ and $\bar{n}_e(r)$ along with snapshots of $n_e(r,t)$ at the phases $t = 0$ and $t = T_{RF}/2$.

Again, the electrons can follow the field, their plasma frequency is $\omega_{pe} = 5.7 \times 10^9\,\mathrm{s}^{-1}$ (center) or $\omega_{pe} =$

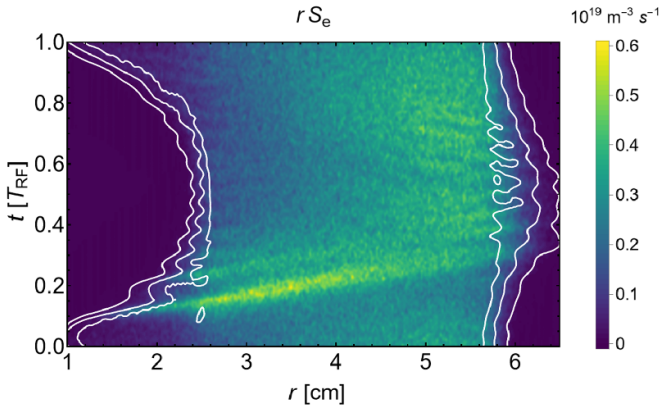

Figure 15. The radially weighted, spatio-temporally resolved profile of the ionization term for the unmagnetized reference discharge.

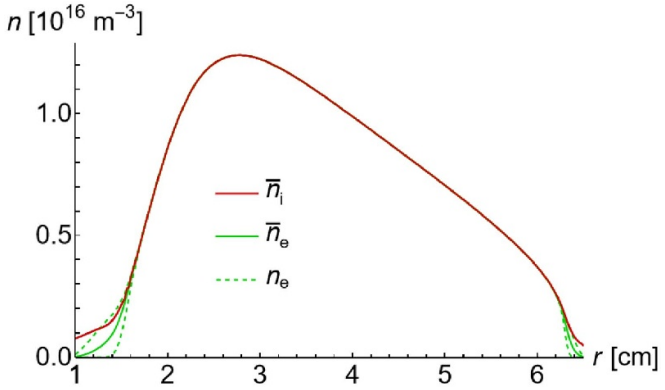

Figure 16. RF period-averaged ion density $\bar{n}_i(r)$ (solid red) and electron density $\bar{n}_e(r)$ (solid green) of the magnetized discharge. The dashed green lines represent the electron densities $n_e(r,t)$ at the moments of electrode sheath minimum ($t=0$) and maximum ($t=T_{RF}/2$), respectively.

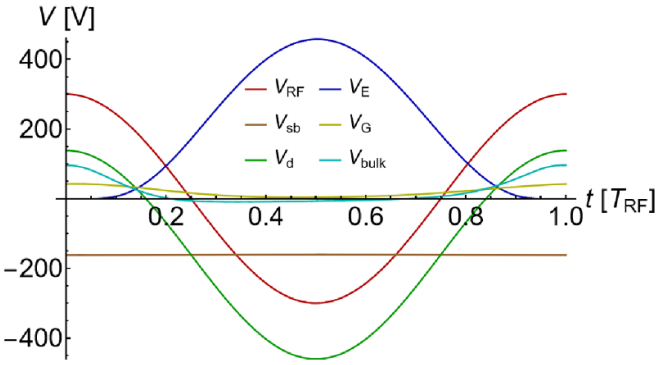

Figure 17. Phase-resolved curves of the applied source voltage $V_{RF}(t)$, the self bias voltage $V_{sb}(t)$, the total discharge voltage $V_d(t)$, the sheath voltages $V_E(t)$ and $V_G(t)$, and the voltage drop $V_{bulk}(t)$ over the plasma bulk for the magnetized case.

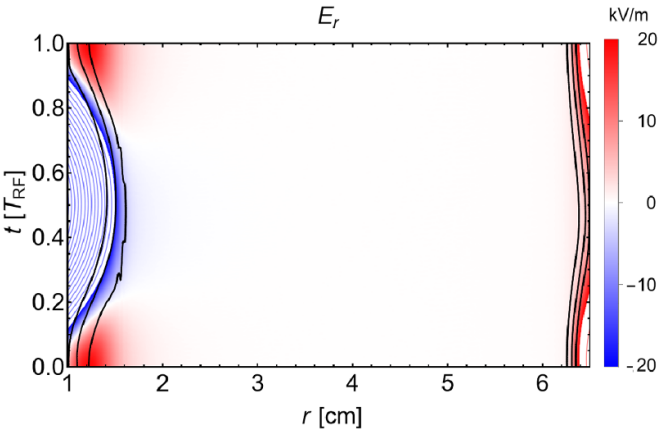

Figure 18. Spatio-temporally resolved electric field $E_r(r,t)$ for the magnetized magnetron discharge. The color shading is scaled to resolve the weak fields in the temporarily quasi-neutral regions; the additional contour lines have a separation of $\Delta E = 20\,\mathrm{kV\,m^{-1}}$.

$2.2\times10^9\,\mathrm{s}^{-1}$ (electrode sheath), while the ion component is essentially unmodulated, $\omega_{pi}=2.1\times10^7\,\mathrm{s}^{-1}$ (center) or $\omega_{pi}=8.1\times10^6\,\mathrm{s}^{-1}$ (electrode sheath). Figure 17 shows the voltages. Figure 18 provides a map of the electric field $E_r(r,t)$.

At first glance, not much has changed compared to unmagnetized reference discharge. The applied voltage $V_{RF}(t)$ is the same. The discharge voltage $V_d(t)$, the sheath voltages $V_E(t)$ and $V_G(t)$, and the self bias $V_{sb}(t)$ are similar. The bulk voltage $V_b(t)$ remains small. Obviously, the discharge is capacitive as well, and the quasi-static analysis (54) still applies. In fact, it is now even more applicable: Because of the higher value of ω_{PSR}, the PSR is no longer excited by the sheath nonlinearities, and the total current $I(t)=2\pi Hrj(r,t)$ is better captured by the quasi-static model or the Drude model, figure 19. As shown in figures 20 and 21, it is carried by the electrons in the bulk and flows as displacement current in the sheaths. (Due to the absence of PSR oscillations, there is almost no displacement current in the bulk.) In contrast to the unmagnetized case, there is now also an azimuthal current j_θ, see figure 22. The waveforms of the sheath charges are similar to those of the unmagnetized case, figure 23. They are, however, larger by a factor of 2. This ratio, which reflects the higher plasma density and the thinner sheaths of the magnetized case, is also visible in the amplitude of the current and in the form of the charge voltage relations $V_E(Q)$ and $V_G(Q)$ shown in figure 24.

The simulation determines the current–voltage phase angle to $\cos\varphi=\cos 83.5^\circ=0.113$ and the dissipated RF power to $\bar{P}=6.76\,\mathrm{W}$. (The Drude model, with $\cos\varphi=\cos 88.8^\circ=0.021$ and $\bar{P}=1.30\,\mathrm{W}$ is far off.) $\bar{P}_i=3.98\,\mathrm{W}$ is taken by the ions, $\bar{P}_e=2.78\,\mathrm{W}$ by the electrons. The power input ratio matches the density ratio, $n_{max}(\mathrm{M})/n_{max}(\mathrm{U})\approx\bar{P}_e(\mathrm{M})/\bar{P}_e(\mathrm{U})\approx 8$. The plasma density of the magnetized case is higher because the heating is more efficient. We will demonstrate that it also has a very different physical character.

As in the unmagnetized reference case, the heating mechanism is related to the electric field in the ambipolar zone which is neglected in the quasi-static analysis and which is only poorly represented by the Drude model, see figure 18. Its

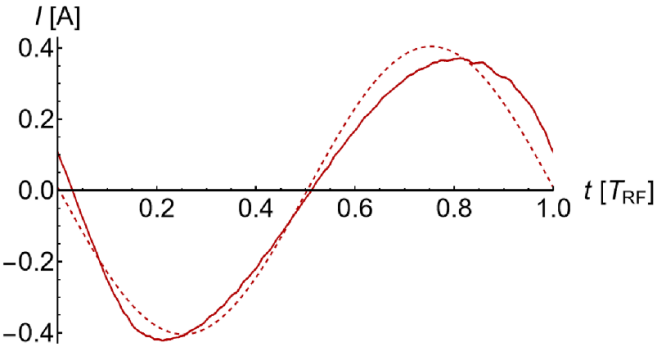

Figure 19. Discharge current $I(t)$ of the magnetized case (solid) in comparison with the discharge current of the corresponding Drude model (dashed).

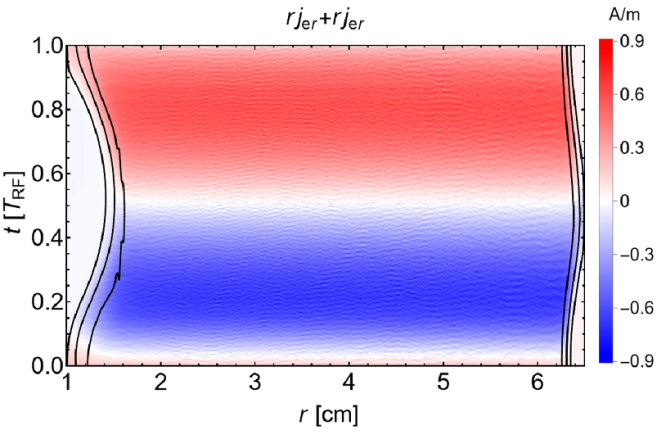

Figure 20. Radially weighted particle current $rj_r(r,t)$ in the magnetized case.

individual components can be analyzed by solving the radial momentum balance (48) with respect to the electric field:

$$\begin{aligned} E_r &= -\frac{1}{en}\left(\frac{\partial}{\partial t}(mnu_r) + \frac{1}{r}\frac{\partial}{\partial r}(rmnu_r^2) - \frac{mnu_\theta^2}{r}\right) \\ &\quad - \frac{1}{ren}\left(\frac{\partial}{\partial r}(rp_{rr}) - p_{\theta\theta}\right) - u_\theta B_z + \frac{F_r}{en} \\ &\equiv E_\mathrm{i} + E_\mathrm{p} + E_\mathrm{H} + E_\mathrm{c}. \end{aligned} \tag{59}$$

The terms on the right can be obtained from the simulation. Two contributions dominate, the pressure field E_p and the Hall field E_H. The pressure field appears at the electron edges of both sheaths and points outward, i.e. is negative around $s_\mathrm{E}(t)$ and positive around $s_\mathrm{G}(t)$. As in the unmagnetized case, it acts as an indicator of the beginning depletion field with which the electrons are roughly in Boltzmann equilibrium. The Hall field E_H reflects the Lorentz force and appears only in the magnetized zone. It has a 180° phase shift with respect to the electron edge s_E. This can be explained in terms of the single-particle picture above: as (34) shows, a positive (reversed) field is needed to move electrons to smaller values of r and a negative one to push them in the opposite direction.) There is thus a positive interference between E_p and E_H at the time of the sheath maximum and a cancellation around time of the sheath

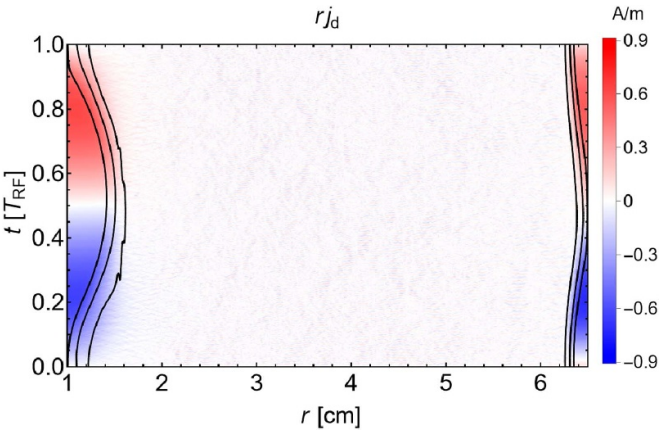

Figure 21. Radially weighted displacement current for the magnetized case.

minimum. However, as E_H is also active where quasineutrality holds, a strong positive field appears during the sheath minimum in the zone $1\,\mathrm{cm} \leqslant r \leqslant 2\,\mathrm{cm}$. The other electric field terms on the right of (59)—reflecting the influence of electron inertia and collisions—are much smaller (see [54]). The dominance of the pressure field and the Hall field can also be detected in figure 25 which displays a phase-resolved map of the radially weighted electron power input $rP_\mathrm{e} = rj_{er}E_r$. Its individual constituents, defined on the basis of the electrical field analysis (59), are displayed in figure 26:

$$\begin{aligned} rP_r &= mu_r\left(r\frac{\partial}{\partial t}(nu_r) + \frac{\partial}{\partial r}\left(rnu_r^2\right) - nu_\theta^2\right) \\ &\quad + u_r\left(\frac{\partial}{\partial r}(rp_{rr}) - p_{\theta\theta}\right) - rj_r u_\theta B_z - ru_r\dot{\pi}_r \\ &\equiv rP_{\mathrm{i}r} + rP_{\mathrm{p}r} + rP_\mathrm{H} + rP_{\mathrm{c}r}. \end{aligned} \tag{60}$$

The pressure term $P_{\mathrm{p}r}$ appears only in the thin transition zones around the electron edges; its value is positive when the sheaths are expanding and negative when they are retracting. The phase average is close to zero. The Hall term P_H is only active in the magnetized region, it is negative just after the sheath collapse and positive just before. The other contributions to the power balance are essentially negligible.

The Hall contribution P_H does not correspond to true power dissipation, as magnetic fields do not do any work and cannot contribute to heating. Instead, the term represents a flow of mechanical energy conducted from radial to azimuthal degrees of freedom and back. This view is supported by the following equation which is obtained by multiplying the azimuthal momentum balance (49) with u_θ:

$$\begin{aligned} renu_\theta u_r B_z &= u_\theta\left(r\frac{\partial}{\partial t}(mnu_\theta) + \frac{1}{r}\frac{\partial}{\partial r}\left(r^2 mnu_r u_\theta\right)\right) \\ &\quad + u_\theta\frac{1}{r}\frac{\partial}{\partial r}\left(r^2 p_{r\theta}\right) - ru_\theta\dot{\pi}_\theta \\ &= rP_{\mathrm{i}\theta} + rP_{\mathrm{p}\theta} + rP_{\mathrm{c}\theta}. \end{aligned} \tag{61}$$

The term on the left is the negative of P_H; it acts as power source for the azimuthal motion. Figure 27 shows the three

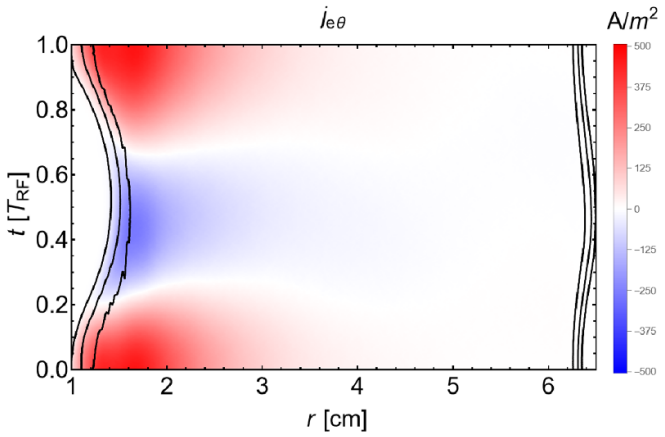

Figure 22. Azimuthal electron current density $j_{e\theta}(r,t)$ for the magnetized case.

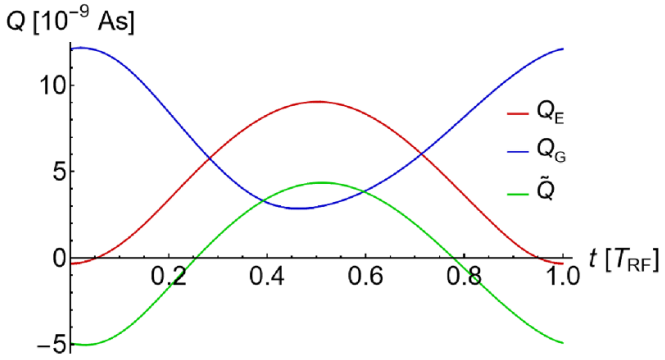

Figure 23. Charges of the electrode sheath $Q_E(t)$ and the ground sheath $Q_G(t)$ together with the average-free integral $\tilde{Q}(t)$ of the current $I(t)$ for the magnetized case.

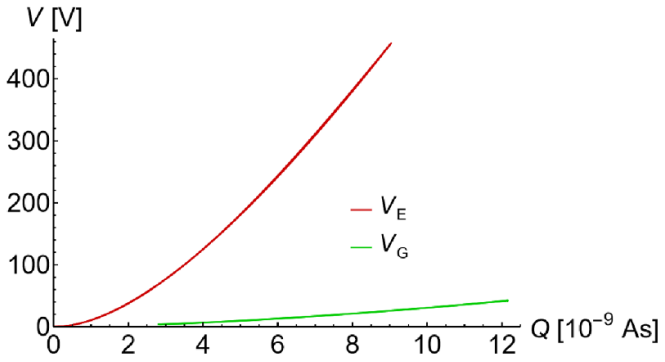

Figure 24. Parametric plot of the electrode sheath voltage $V_E(t)$ and the ground sheath voltage $V_E(t)$ versus the sheath charges $Q(t)$ for the magnetized case.

contributions on the right. To begin with the least important one: the term $P_{p\theta}$ reflects the shear component of the pressure tensor and is linked to the collisionless effect of gyroviscosity: radial transport of the axial momentum component caused by electron gyration [79]. Physically, and by numerical value, it is rather insignificant. The term $P_{i\theta}$ is associated with electron inertia and reflects the periodic acceleration and deceleration

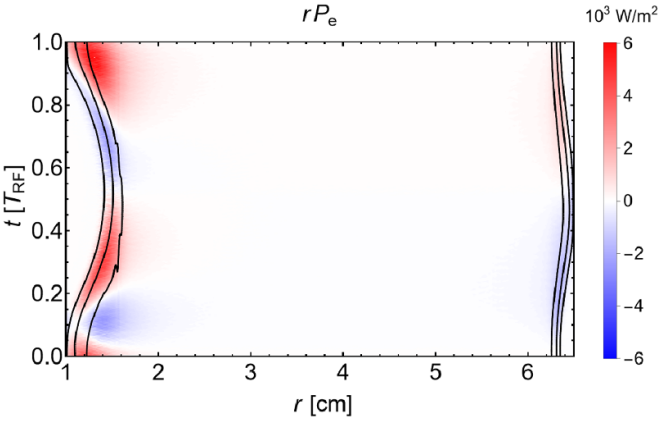

Figure 25. The radially weighted spatio-temporally resolved electron power absorption.

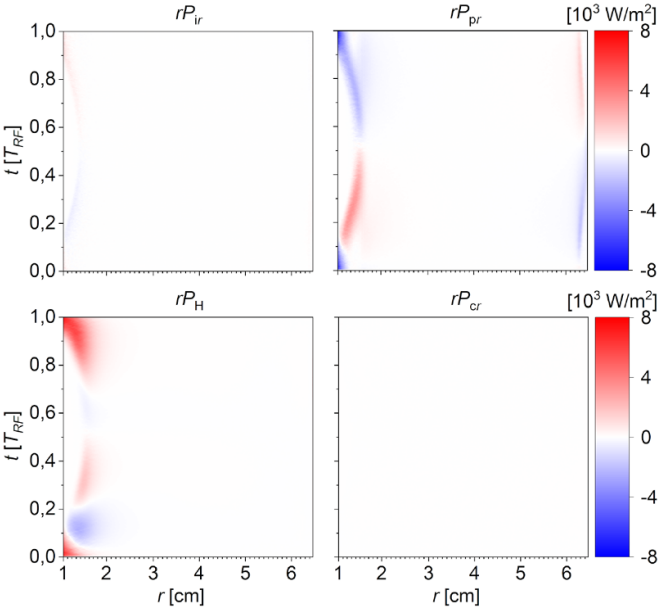

Figure 26. The radially weighted spatio-temporally resolved constituents from (60) of the power dissipation.

of the electrons related to the $\boldsymbol{E}\times\boldsymbol{B}$ drift. During the field growth before the sheath collapse, energy is transferred to the electrons; after the collapse, is transferred back. This energizing mechanism is collisionless; it was already captured in the single-particle view. It generates a strong electron beam in the azimuthal direction, with a velocity that may exceed the thermal velocity significantly. (Even if the drift speed $v_{E\times B}$ is not larger than the thermal velocity but comparable to it, the kinetic energy can be up to four times larger than the thermal energy alone when the gyro motion and the drift have the same direction.) A sizable number of electrons close to the powered electrode can therefore reach energies in the inelastic range, so that they can participate directly in excitation or ionization processes. This is seen in the term $P_{c\theta}$ and in the ionization rate shown in figure 28. The confining effect of the magnetic field prevents the electrons from being ejected from the magnetized

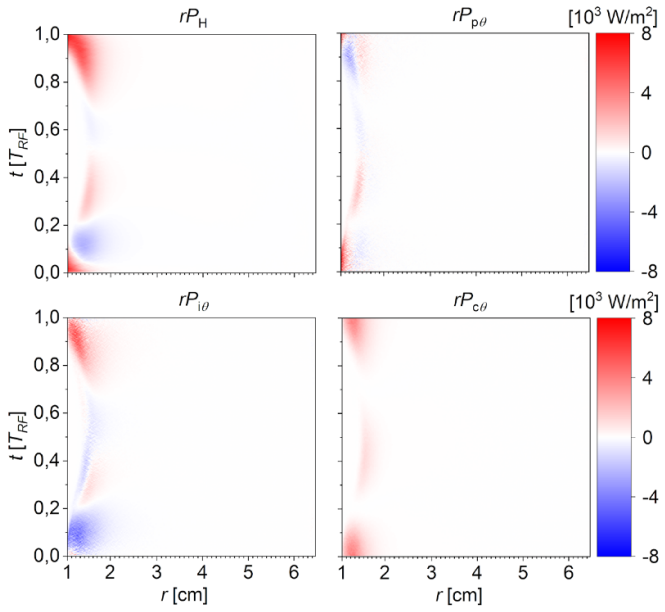

Figure 27. The spatio-temporally resolved Hall power and its constituents.

zone, allowing them to experience large electric fields over a long period of time. Note that the number of energetic electrons in such a zone is increased by the production of new electrons via the ionization process. Such electrons experience the same strong electric field and thus gain the same large $\mathbf{E}\times\mathbf{B}$ azimuthal drift velocity resulting in a large total kinetic energy. Under a sufficiently large ionization probability during a time interval when an electron feels a large electric field close to the powered electrode, this might significantly enhance the ionization efficiency by creating an ionization avalanche.

The findings are supported by the graphs of figure 29, which illustrate the electron velocity distribution in the (v_r, v_θ) plane of the velocity space for different phases of the RF cycle. The electrons were sampled from a segment close to the powered electrode, $1\,\mathrm{cm} \leqslant r \leqslant 2\,\mathrm{cm}$, where most of the energetic electrons are produced. (Secondary electrons are not shown.) The velocity range is the interval $[-v_{\max}, v_{\max}]$, $v_{\max} = 4.2\times10^6\,\mathrm{m\,s^{-1}}$ corresponds to 50 eV. The boundary between the elastic and inelastic energy range is shown as a magenta circle. At $t=0$, all electrons experience a strong positive ('reversed') electric field which generates a fast $\boldsymbol{E}\times\boldsymbol{B}$ drift in the negative θ direction (figure 29(a)). A substantial fraction of electrons is pushed beyond the inelastic energy threshold. When the powered electrode sheath expands—we chose the moment $t = 0.25\,T_{\mathrm{RF}}$ —, the electric field at the sheath edge changes polarity and the $\boldsymbol{E}\times\boldsymbol{B}$ drift becomes small for the electrons close to the expanding sheath edge. The corresponding distribution of energetic electrons becomes symmetric in v_θ (figure 29(b)). Finally, at $t = 0.5\,T_{\mathrm{RF}}$, when the powered sheath is maximal, electrons at the sheath edge experience a strong negative electric field. The fast $\boldsymbol{E}\times\boldsymbol{B}$ drift in the positive θ direction generates a large number of energetic electrons. Electrons closer to the bulk experience only a weak electric field, so their distribution, which dominates

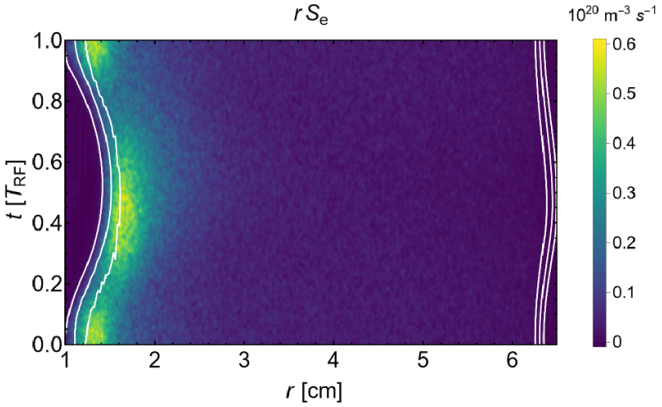

Figure 28. Radially weighted ionization rate rS_e for the magnetized discharge.

the low-energy part, is symmetric. The slight asymmetry of the energetic tail with respect to v_r (figure 29(b)) can be attributed to magnetized stochastic heating [40]. The effects is much weaker than Hall heating.

The described mechanisms are also seen the figure which shows the phase-resolved electron energy probability functions (EEPFs) in the three directions extracted from the simulation. (In each case, the full EEPF was integrated over the other directions.) The azimuthal EEPF_θ shows the most pronounced modulation. Its energetic phases are at $t=0$ and $t = T_{\mathrm{RF}}/2$, clearly related to the maxima of the $\boldsymbol{E}\times\boldsymbol{B}$-drift during sheath collapse and sheath expansion. The radial EEPF_r is less modulated; the magnetized sheath heating (as proposed in [40]) and the isotropizing effect of collisions are relatively weak. The axial EEPF_z, finally, stays nearly constant, it is only influenced by the collisions.

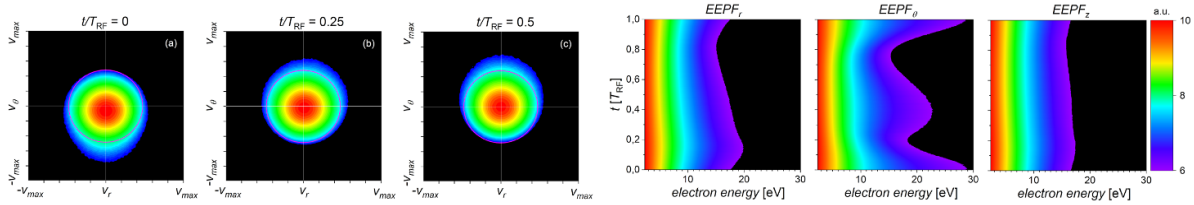

Figure 29. Visualization of the electron distribution function, showing the dynamics of the μ-mode. Top: distribution in the (v_r, v_θ) plane of the velocity space sampled at three different RF phases. The magenta circle corresponds to the first excitation level of argon at 11.5 eV and indicates the boundary of the inelastic energy range. Bottom: phase-resolved electron energy probability function EEPF in the coordinate directions. Secondary electrons are not displayed.

8. Summary and conclusions

In this study, we investigated the electron dynamics and the mechanisms of power absorption in a RF-driven, MECCP. The device in focus was a deliberately simplified representation of a planar RF magnetron, namely an infinitely long cylindrical magnetron with a radially nonuniform magnetic field in axial direction and an electric field in radial direction. The applied voltage was $V_{\mathrm{RF}} = 300\,\mathrm{V}$, the gas argon at a pressure of $p = 0.5\,\mathrm{Pa}$. An unmagnetized discharge of the same geometry and operation conditions was used for comparison. The dynamics was studied analytically with the cold plasma model and a single-particle formalism, and numerically with the inhouse energy and charge conserving PIC/MCC code ECCOPIC1S-M.

The reference discharge showed the well-known mechanisms of pressure heating, NERH, and, to a lesser extent, Ohmic heating, all acting mainly in the vicinity of the powered sheath. The magnetized CCP, in contrast, operates by means of a significantly more efficient power absorption mechanism, which we named 'Hall heating'. It is caused by the discharge's need to ensure the electron current continuity against the inhibitory effect of the magnetic field. A single-particle study emphasized the role of polarization drift in cross-field transport. The required strong electric field has a phase shift of 180° compared to the electron edge s_{E}; it is negative when the sheath width is maximal and positive (reversed) when it is minimal. The corresponding strong azimuthal $\mathbf{E}\times\mathbf{B}$-drift then constitutes the 'Hall heating' as such. It is by a factor $\omega_{\mathrm{ce}}/\omega_{\mathrm{RF}}$ larger than the polarization drift and can accelerate a relatively large number of electrons into the inelastic energy range. These electrons—which are drawn not only from the vicinity of the electron edge but also from momentarily quasineutral regions—can either directly participate in inelastic processes such as impact ionization or convert their kinetic energy into random motion through elastic collisions. Hall heating is different from the heating mechanism proposed by Lieberman, Lichtenberg, and Savas [40], as it does not rely on multiple collisions with the expanding sheath. It also differs from Ohmic heating; since it is not a matter of a diffusion process in energy space. It is something entirely new. We propose to call it the 'μ-mode', to separate it from other discharge heating modes. Contribution of this mechanism to the production of energetic electrons participating in the ionization processes can be significantly enhanced due to the fact that the electrons created in the ionization will be energized by the same mechanism via gaining a strong azimuthal $\mathbf{E}\times\mathbf{B}$ drift, which may result in an ionization avalanche. A companion study [56] will investigate the newly described mechanism in a more realistic planar magnetron geometry and focus also on the electron motion along the magnetic field. A second companion study [57] will present experimental observations obtained in a planar RF magnetron and interpret them with help of the newly gained knowledge.

Data availability statement

All data that support the findings of this study are included within the article (and any supplementary files).

Acknowledgments

The authors gratefully acknowledge support by DFG (German Research Foundation) within the framework of the Sonderforschungsbereich SFB-TR 87 and the Project 'Plasmabasierte Prozessführung von reaktiven Sputterprozessen' No. 417888799.

Appendix. Approximate solution of the equations of motion

The electron motion in the cross-sectional r–θ plane under the influence of a static magnetic field $\boldsymbol{B} = B_z(r)\boldsymbol{e}_z$ and a dynamic electric field $\boldsymbol{E} = E_r(r,t)\boldsymbol{e}_r$ can be viewed as an interplay between gyrorotation and drift. For a dimensionless notation, we employ the length scale L of the system and the time scale T of the applied RF excitation and write the fields and the particle coordinates as

$$E_r(r,t) = \frac{1}{\eta}\frac{m_{\mathrm{e}}L}{eT^2}\tilde{E}(r/L, t/T)\,, \tag{A1}$$

$$B_z(r) = \frac{1}{\eta}\frac{m_{\mathrm{e}}}{eT}\tilde{B}(r/L)\,, \tag{A2}$$

$$r(t) = L\tilde{r}(t/T), \tag{A3}$$

$$\theta(t) = \tilde{\theta}(t/T), \tag{A4}$$

$$v_r(t) = \frac{L}{T}\tilde{v}_r(t/T), \tag{A5}$$

$$v_\theta(t) = \frac{L}{T}\tilde{v}_\theta(t/T). \tag{A6}$$

The quantity $\eta \approx 0.1$ (in the magnetized region) is a dimensionless smallness parameter. The adopted scaling causes the gyromotion to be fast compared to the RF frequency,

$$\omega_{ce} = \frac{eB_z}{m_e} = \frac{1}{\eta}\frac{1}{T}\tilde{B} \sim \frac{1}{\eta T}, \tag{A7}$$

and the $E \times B$ drift comparable to the thermal speed which is of order L/T,

$$v_{E\times B} = \frac{E_r}{B_z} = \frac{\tilde{E}}{\tilde{B}}\frac{L}{T} \sim \frac{L}{T}. \tag{A8}$$

Switching to dimensionless space and time coordinates, $r \to L\tilde{r}$ and $t \to T\tilde{t}$, and then dropping the tilde, we formulate the equations of motion as

$$\frac{\mathrm{d}r}{\mathrm{d}t} = v_r, \tag{A9}$$

$$\frac{\mathrm{d}v_r}{\mathrm{d}t} = -\frac{1}{\eta}\big(E(r,t) + B(r)v_\theta\big) + \frac{v_\theta^2}{r}, \tag{A10}$$

$$\frac{\mathrm{d}\theta}{\mathrm{d}t} = \frac{v_\theta}{r}, \tag{A11}$$

$$\frac{\mathrm{d}v_\theta}{\mathrm{d}t} = \frac{1}{\eta}B(r)v_r - \frac{v_\theta v_r}{r}. \tag{A12}$$

We introduce the flux function $\Psi(r)$ which is related to the vector potential A_θ,

$$\Psi(r) = \int_0^r B(r')\,r'\mathrm{d}r' = rA_\theta(r), \tag{A13}$$

and express the magnetic field as

$$B(r) = \frac{1}{r}\frac{\partial \Psi}{\partial r}. \tag{A14}$$

Owing to the cylindrical symmetry of the configuration, there is an exact constant of motion, the canonical momentum p_θ in θ direction. It is used to define a reference radius $\hat{r}$:

$$p_\theta = rv_\theta - \frac{1}{\eta}\Psi(r) \stackrel{!}{=} -\frac{1}{\eta}\Psi(\hat{r}). \tag{A15}$$

The electric and magnetic fields at the reference radius $\hat{r}$ are also denoted by a circumflex; the spatial derivatives with an additional prime:

$$\hat{E}(t) = E(\hat{r},t)\,, \tag{A16}$$

$$\hat{B} = B(\hat{r})\,, \tag{A17}$$

$$\hat{E}'(t) = \frac{\partial E}{\partial r}(\hat{r},t)\,, \tag{A18}$$

$$\hat{B}' = \frac{\partial B}{\partial r}(\hat{r})\,. \tag{A19}$$

Equation (A15) can be used to eliminate the variable v_θ via

$$v_\theta = \frac{\Psi(r) - \Psi(\hat{r})}{\eta\, r}. \tag{A20}$$

The remaining equations are then

$$\frac{\mathrm{d}r}{\mathrm{d}t} = v_r, \tag{A21}$$

$$\frac{\mathrm{d}\theta}{\mathrm{d}t} = \frac{\Psi(r) - \Psi(\hat{r})}{\eta\, r^2}, \tag{A22}$$

$$\frac{\mathrm{d}v_r}{\mathrm{d}t} = -\frac{E(r,t)}{\eta} + \frac{(\Psi(r) - \Psi(\hat{r}))^2}{\eta^2 r^3} - \frac{(\Psi(r) - \Psi(\hat{r}))\Psi'(r)}{\eta^2 r^2}. \tag{A23}$$

To account for the time scale disparity, we distinguish between the fast gyroscale $t_f = \eta t$ and the slower RF scale $t_s = t$. Splitting the time derivative accordingly, we obtain:

$$\frac{1}{\eta}\frac{\partial r}{\partial t_f} + \frac{\partial r}{\partial t_s} = v_r, \tag{A24}$$

$$\frac{1}{\eta}\frac{\partial \theta}{\partial t_f} + \frac{\partial \theta}{\partial t_s} = \frac{\Psi(r) - \Psi(\hat{r})}{\eta\, r^2}, \tag{A25}$$

$$\frac{1}{\eta}\frac{\partial v_r}{\partial t_f} + \frac{\partial v_r}{\partial t_s} = -\frac{E(r,t_s)}{\eta} + \frac{(\Psi(r) - \Psi(\hat{r}))^2}{\eta^2 r^3} - \frac{(\Psi(r) - \Psi(\hat{r}))\Psi'(r)}{\eta^2 r^2}. \tag{A26}$$

We now make a power series ansatz in η, displaying only those terms that are actually used. Note that the leading order of r is fixed to be the reference radius $\hat{r}$:

$$r(t_f,t_s) = \hat{r} + \eta\, r^{(1)}(t_f,t_s) + \eta^2\, r^{(2)}(t_f,t_s) + \ldots, \tag{A27}$$

$$\theta(t_f,t_s) = \theta^{(0)}(t_f,t_s) + \eta\,\theta^{(1)}(t_f,t_s) + \ldots, \tag{A28}$$

$$v_r(t_f,t_s) = v_r^{(0)}(t_f,t_s) + \eta\, v_r^{(1)}(t_f,t_s) + \ldots. \tag{A29}$$

Expanding the equations of motion into a Taylor series in the smallness parameter η and sorting for powers gives a hierarchy of equations. In leading order, they are:

$$\frac{\partial r^{(1)}}{\partial t_f} - v_r^{(0)} = 0, \tag{A30}$$

$$\frac{\partial \theta^{(0)}}{\partial t_f} = 0, \tag{A31}$$

$$\frac{\partial v_r^{(0)}}{\partial t_\mathrm{f}} + \hat{B}^2 r^{(1)} = -\hat{E}(t_\mathrm{s}). \tag{A32}$$

This system can readily be solved. The integration constants ρ, $\hat{\phi}$, and $\hat{\theta}$ may still depend on the slow time t_s (which we suppress in the notation for brevity):

$$r^{(1)}(t_\mathrm{f}, t_\mathrm{s}) = \rho\cos\big(\hat{B}t_\mathrm{f} + \hat{\phi}\big) - \frac{\hat{E}}{\hat{B}^2}, \tag{A33}$$

$$\theta^{(0)}(t_\mathrm{f}, t_\mathrm{s}) = \hat{\theta}, \tag{A34}$$

$$v_r^{(0)}(t_\mathrm{f}, t_\mathrm{s}) = -\hat{B}\rho\cos\big(\hat{B}t_\mathrm{f} + \hat{\phi}\big). \tag{A35}$$

The dynamical equations of the next order appear as inhomogeneous differential equations for the quantities $r^{(2)}$, $\theta^{(1)}$, and $v_r^{(1)}$. Note that the homogeneous part is formally identical to the equations of the leading order:

$$\begin{aligned}\frac{\partial r^{(2)}}{\partial t_\mathrm{f}} - v_r^{(1)} = \frac{1}{\hat{B}^2}\frac{\partial \hat{E}}{\partial t_\mathrm{s}} - \cos\big(\hat{B}t_\mathrm{f} + \hat{\phi}\big)\frac{\partial \rho}{\partial t_\mathrm{s}} \\ + \rho\sin\big(\hat{B}t_\mathrm{f} + \hat{\phi}\big)\frac{\partial \phi}{\partial t_\mathrm{s}},\end{aligned} \tag{A36}$$

$$\frac{\partial \theta^{(1)}}{\partial t_\mathrm{f}} = -\frac{\partial \hat{\theta}}{\partial t_\mathrm{s}} + \frac{\hat{B}}{\hat{r}}\rho(t_\mathrm{s})\cos\big(\hat{B}t_\mathrm{f} + \hat{\phi}\big) - \frac{\hat{E}}{\hat{r}\hat{B}}, \tag{A37}$$

$$\begin{aligned}\frac{\partial v_r^{(1)}}{\partial t_\mathrm{f}} + \hat{B}^2 r^{(2)} = \frac{\hat{E}\hat{E}'}{\hat{B}^2} + \frac{3}{2}\left(\frac{1}{\hat{r}} - \frac{\hat{B}'}{\hat{B}}\right)\frac{\hat{E}^2}{\hat{B}^2} \\ + \left(3\left(\frac{\hat{B}'}{B} - \frac{1}{\hat{r}}\right)\hat{E} - \hat{E}'\right)\rho\cos\big(\hat{B}t_\mathrm{f} + \hat{\phi}\big) \\ + \left(\frac{3\hat{B}^2}{4\hat{r}} - \frac{3\hat{B}\hat{B}'}{4}\right)\rho^2 + \left(\frac{3\hat{B}^2}{4\hat{r}} - \frac{3\hat{B}\hat{B}'}{4}\right) \\ \times\rho^2\cos\Big(2\big(\hat{B}t_\mathrm{f} + \hat{\phi}\big)\Big) \\ + \hat{B}\left(\sin\big(\hat{B}t_\mathrm{f} + \hat{\phi}\big)\frac{\partial \rho}{\partial t_\mathrm{s}} + \rho\cos\big(\hat{B}t_\mathrm{f} + \hat{\phi}\big)\frac{\partial \hat{\phi}}{\partial t_\mathrm{s}}\right).\end{aligned} \tag{A38}$$

When solving these equations, care must be taken to avoid terms that linearly diverge in t_f. This poses consistency conditions on the inhomogeneous terms on the right, which can be solved for the evolution equations for the integration constants ρ, $\hat{\phi}$, and $\hat{\theta}$ in the time t_s. It turns out that ρ is a constant altogether. (This fact is related to the adiabatic constancy of the magnetic moment $\mu = v_\perp^2/2B$ which is valid for drift theories under general conditions.) The angles $\hat{\phi}$, and $\hat{\theta}_0$, in contrast, exhibit slow drifts:

$$\frac{\partial \rho}{\partial t_\mathrm{s}} = 0, \tag{A39}$$

$$\frac{\partial \hat{\phi}}{\partial t_\mathrm{s}} = \frac{3}{2}\left(\frac{1}{\hat{B}\hat{r}} - \frac{\hat{B}'}{\hat{B}^2}\right)\hat{E} + \frac{1}{2\hat{B}}\hat{E}', \tag{A40}$$

$$\frac{\partial \hat{\theta}}{\partial t_\mathrm{s}} = -\frac{\hat{E}}{\hat{B}\hat{r}}. \tag{A41}$$

Under this condition, the next order quantities can be calculated as

$$\begin{aligned}r^{(2)}(t_\mathrm{f}, t_\mathrm{s}) = \frac{\hat{E}\hat{E}'}{\hat{B}^4} - \frac{3\hat{B}'\hat{E}^2}{2\hat{B}^5} + \frac{3\hat{E}^2}{2\hat{B}^4\hat{r}} \\ + \left(\frac{3\hat{B}'\hat{E}}{4\hat{B}^3} - \frac{\hat{E}'}{4\hat{B}^2} - \frac{3\hat{E}}{4\hat{B}^2\hat{r}}\right)\rho\cos\big(\hat{B}t_\mathrm{f} + \hat{\phi}\big) \\ + \left(-\frac{3\hat{B}'}{4\hat{B}} + \frac{3}{4\hat{r}} + \left(\frac{\hat{B}'}{4\hat{B}} - \frac{1}{4\hat{r}}\right)\right. \\ \left.\times\rho^2\cos\Big(2\big(\hat{B}t_\mathrm{f} + \hat{\phi}\big)\Big)\right) \\ + \rho_a\cos\big(\hat{B}t_\mathrm{f} + \phi\big) + \rho_b\sin\big(\hat{B}t_\mathrm{f} + \hat{\phi}\big),\end{aligned} \tag{A42}$$

$$\theta^{(1)}(t_\mathrm{f}, t_\mathrm{s}) = \frac{1}{\hat{r}}\rho\sin\big(\hat{B}t_\mathrm{f} + \hat{\phi}\big) + \hat{\theta}_1, \tag{A43}$$

$$\begin{aligned}v_r^{(1)}(t_\mathrm{f}, t_\mathrm{s}) = -\frac{1}{\hat{B}^2}\frac{\partial \hat{E}}{\partial t_\mathrm{s}} + \left(\frac{3\hat{B}'\hat{E}}{4\hat{B}^2} - \frac{\hat{E}'}{4\hat{B}} - \frac{3\hat{E}}{4\hat{B}\hat{r}}\right)\rho\sin\big(\hat{B}t_\mathrm{f} + \hat{\phi}\big) \\ + \left(\frac{\hat{B}}{2\bar{r}} - \frac{\hat{B}'}{2}\right)\rho^2\sin\Big(2\big(\hat{B}t_\mathrm{f} + \hat{\phi}\big)\Big) \\ + \hat{B}\left(\rho_b\cos\big(\hat{B}t_\mathrm{f} + \hat{\phi}\big) - \rho_a\sin\big(\hat{B}t_\mathrm{f} + \hat{\phi}\big)\right).\end{aligned} \tag{A44}$$

Using rule (A20), the first two orders of the azimuth velocity v_θ can be reconstructed as

$$v_\theta^{(0)}(t_\mathrm{f}, t_\mathrm{s}) = -\frac{\hat{E}}{\hat{B}} + \hat{B}\rho\cos\big(\hat{B}t_\mathrm{f} + \hat{\phi}\big), \tag{A45}$$

$$\begin{aligned}v_\theta^{(1)}(t_\mathrm{f}, t_\mathrm{s}) = \frac{\hat{E}\hat{E}'}{\hat{B}^3} - \frac{\hat{B}'\hat{E}^2}{\hat{B}^4} + \frac{\hat{E}^2}{\hat{B}^3\hat{r}} \\ + \left(-\frac{\hat{B}'\hat{E}}{4\hat{B}^2} - \frac{\hat{E}'}{4\hat{B}} + \frac{\hat{E}}{4\hat{B}\hat{r}}\right)\rho\cos\big(\hat{B}t_\mathrm{f} + \hat{\phi}\big) \\ + \rho^2\left(-\frac{\hat{B}'}{2} + \frac{\hat{B}}{2\hat{r}} + \left(\frac{\hat{B}'}{2} - \frac{\hat{B}}{2\hat{r}}\right)\cos\Big(2\big(\hat{B}t_\mathrm{f} + \hat{\phi}\big)\Big)\right) \\ + \hat{B}\left(\rho_a\cos\big(\hat{B}t_\mathrm{f} + \hat{\phi}\big) + \rho_b\sin\big(\hat{B}t_\mathrm{f} + \hat{\phi}\big)\right).\end{aligned} \tag{A46}$$

In order to construct the most economical representation possible for the electron trajectory, we proceed as follows. First, we note that the leading order of the expansion can absorb the homogeneous part of the higher order by redefinition of the integration constants ρ, $\hat{\phi}$, and $\hat{\theta}$. Second, we restrict ourselves to contributions of first order in either gyromotion or drift. This leads to the form:

$$r(t_\mathrm{f}, t_\mathrm{s}) = \hat{r} + \eta\left(\rho\cos\big(\hat{B}t_\mathrm{f} + \hat{\phi}\big) - \frac{\hat{E}}{\hat{B}^2}\right), \tag{A47}$$

$$\theta(t_\mathrm{f}, t_\mathrm{s}) = \hat{\theta} + \eta\frac{1}{\hat{r}}\rho\sin\big(\hat{B}t_\mathrm{f} + \hat{\phi}\big), \tag{A48}$$

$$v_r(t_\mathrm{f}, t_\mathrm{s}) = -\hat{B}\rho\cos\left(\hat{B}t_\mathrm{f} + \hat{\phi}\right) - \eta\frac{1}{\hat{B}^2}\frac{\partial\hat{E}}{\partial t_\mathrm{s}}, \tag{A49}$$

$$v_\theta(t_\mathrm{f}, t_\mathrm{s}) = -\frac{\hat{E}}{\hat{B}} + \hat{B}\rho\cos\left(\hat{B}t_\mathrm{f} + \hat{\phi}\right). \tag{A50}$$

For the integration constants, we have the slow drift

$$\frac{\partial\hat{\phi}}{\partial t_\mathrm{s}} = \frac{3}{2}\left(\frac{1}{B\hat{r}} - \frac{B'}{B^2}\right)\hat{E} + \frac{1}{2B}\hat{E}', \tag{A51}$$

$$\frac{\partial\hat{\theta}}{\partial t_\mathrm{s}} = -\frac{\hat{E}}{\hat{B}\hat{r}}. \tag{A52}$$

Lastly, we remove the two-timescale formalism and the normalization to obtain the desired approximation of the electron trajectories:

$$r(t) = \hat{r} - \frac{m_\mathrm{e}\hat{E}}{e\hat{B}_r^2} + \rho\cos\left(\frac{e\hat{B}}{m_\mathrm{e}}t + \hat{\phi}\right), \tag{A53}$$

$$\theta(t) = \hat{\theta} + \frac{\rho}{\hat{r}}\sin\left(\frac{e\hat{B}}{m_\mathrm{e}}t + \hat{\phi}\right), \tag{A54}$$

$$v_r(t) = -\frac{m_\mathrm{e}}{e\hat{B}^2}\frac{\partial\hat{E}}{\partial t_\mathrm{s}} - \frac{e\hat{B}}{m_\mathrm{e}}\rho\cos\left(\frac{e\hat{B}}{m_\mathrm{e}}t + \hat{\phi}\right), \tag{A55}$$

$$v_\theta(t) = -\frac{\hat{E}}{\hat{B}} + \frac{e\hat{B}}{m_\mathrm{e}}\rho\cos\left(\frac{e\hat{B}}{m_\mathrm{e}}t + \hat{\phi}\right). \tag{A56}$$

The parameters $\hat{r}$ and ρ are constants; the parameters $\hat{\phi}$ and $\hat{\theta}$ follow drift equations:

$$\frac{\partial\hat{\phi}}{\partial t} = \frac{3}{2}\left(\frac{1}{\hat{B}\hat{r}} - \frac{\hat{B}'}{\hat{B}^2}\right)\hat{E} + \frac{1}{2\hat{B}}\hat{E}', \tag{A57}$$

$$\frac{\partial\hat{\theta}}{\partial t} = -\frac{\hat{E}}{\hat{B}\hat{r}}. \tag{A58}$$

By introducing the reference gyrofrequency $\hat{\Omega} = e\hat{B}/m_\mathrm{e}$, the drift velocity $\hat{v}_{E\times B} = \hat{E}/\hat{B}$, and its spatial derivative $\hat{v}'_{E\times B} = \hat{E}/\hat{B}'$, the representation of a trajectory can be written

$$r(t) = \hat{r} - \frac{\hat{v}_{E\times B}}{\hat{\Omega}} + \rho\cos\left(\hat{\Omega}t + \hat{\phi}\right), \tag{A59}$$

$$\theta(t) = \hat{\theta} + \frac{\rho}{\hat{r}}\sin\left(\hat{\Omega}t + \hat{\phi}\right), \tag{A60}$$

$$v_r(t) = -\frac{1}{\hat{\Omega}}\frac{\mathrm{d}\hat{v}_{E\times B}}{\mathrm{d}t} - \hat{\Omega}\rho\cos\left(\hat{\Omega}t + \hat{\phi}\right), \tag{A61}$$

$$v_\theta(t) = -\hat{v}_{E\times B} + \hat{\Omega}\rho\cos\left(\hat{\Omega} + \hat{\phi}\right), \tag{A62}$$

and the drift equations for the integration constants read:

$$\frac{\partial\hat{\phi}}{\partial t} = \frac{3}{2}\left(\frac{1}{\hat{r}} - \frac{\hat{B}'}{\hat{B}}\right)\hat{v}_{E\times B} + \frac{1}{2}\hat{v}'_{E\times B}, \tag{A63}$$

$$\frac{\partial\hat{\theta}}{\partial t} = -\frac{\hat{v}_{E\times B}}{\hat{r}}. \tag{A64}$$

ORCID iDs

Denis Eremin https://orcid.org/0000-0001-5160-6385
Dennis Krüger https://orcid.org/0000-0003-2532-0193
Sebastian Wilczek https://orcid.org/0000-0003-0583-4613
Andrei Smolyakov https://orcid.org/0000-0002-4975-2743
Julian Schulze https://orcid.org/0000-0001-7929-5734

References

[1] Lieberman M and Lichtenberg A 2005 *Principles of Plasma Discharges and Materials Processing* 2nd edn (New York: Wiley)
[2] Thornton J and Penfold A 1978 *Thin Film Processes* ed L Vossen and K Kern (New York: Academic)
[3] Chapman B 1980 *Glow Discharge Processes* (New York: Wiley)
[4] Lin I, Hinson D, Class W and Sandstrom R 1984 *Appl. Phys. Lett.* **44** 185
[5] Depla D and Mahieu S 2008 *Reactive Sputter Deposition* (Berlin: Springer)
[6] Manos D and Flamm D 1989 *Plasma Etching - An Introduction* (New York: Academic)
[7] Hagelaar G and Oudini N 2011 *Plasma Phys. Control. Fusion* **53** 124032
[8] Thornton J 1981 *Thin Solid Films* **80** 1
[9] Piel A 2017 *Plasma Physics* (Berlin: Springer)
[10] Kushner M 2003 *J. Appl. Phys.* **94** 1436
[11] Rossnagel S 2020 *J. Vac. Sci. Technol.* A **38** 060805
[12] Boeuf J-P and Smolyakov A 2018 *Phys. Plasmas* **25** 061001
[13] Kaganovich I *et al* 2020 *Phys. Plasmas* **27** 120601
[14] Anders A 2014 *Appl. Phys. Lett.* **105** 244104
[15] Tsendin L 2011 *Plasma Sources Sci. Technol.* **20** 055011
[16] Kudryavtsev A, Smirnov A and Tsendin L 2010 *Physics of Glow Discharge* (in Russian) (Saint Petersburg: Lan')
[17] Godyak V 1972 *Sov. Phys.-Tech. Phys.* **16** 1073
[18] Lieberman M and Godyak V 1998 *IEEE Trans. Plasma Sci.* **26** 955
[19] Kaganovich I, Kolobov V and Tsendin L 1996 *Appl. Phys. Lett.* **69** 3818
[20] Lafleur T and Chabert P 2015 *Plasma Sources Sci. Technol.* **24** 044002
[21] Gozadinos G, Turner M and Vender D 2001 *Phys. Rev. Lett.* **87** 135004
[22] Schulze J, Donkó Z, Derzsi A, Korolov I and Schuengel E 2015 *Plasma Sources Sci. Technol.* **24** 015019
[23] Turner M 2009 *J. Phys. D: Appl. Phys.* **42** 194008
[24] Lafleur T, Chabert P, Turner M and Booth J 2014 *Plasma Sources Sci. Technol.* **23** 015016
[25] Schulze J, Donkó Z, Lafleur T, Wilczek S and Brinkmann R 2018 *Plasma Sources Sci. Technol.* **27** 055010
[26] Sato A and Lieberman M 1990 *J. Appl. Phys.* **68** 6117
[27] Vender D and Boswell R 1992 *J. Vac. Sci. Technol.* A **10** 1331
[28] Tochikubo F, Makabe T, Kakuta S and Suzuki A 1992 *J. Appl. Phys.* **71** 2143
[29] Schulze J, Donkó Z, Heil B, Luggenhölscher D, Mussenbrock T, Brinkmann R and Czarnetzki U 2008 *J. Phys. D: Appl. Phys.* **41** 105214
[30] Eremin D, Hemke T and Mussenbrock T 2015 *Plasma Sources Sci. Technol.* **24** 044004
[31] Czarnetzki U, Mussenbrock T and Brinkmann R 2006 *Phys. Plasmas* **13** 123503
[32] Mussenbrock T, Brinkmann R, Lieberman M, Lichtenberg A and Kawamura E 2008 *Phys. Rev. Lett.* **101** 085004
[33] Lieberman M, Lichtenberg A, Kawamura E, Mussenbrock T and Brinkmann R 2008 *Phys. Plasmas* **15** 063505

[34] Donkó Z, Schulze J, Czarnetzki U and Luggenhölscher D 2009 *Appl. Phys. Lett.* **94** 131501
[35] Wilczek S *et al* 2016 *Phys. Plasmas* **23** 063514
[36] Wilczek S, Trieschmann J, Schulze J, Donkó Z, Brinkmann R and Mussenbrock T 2018 *Plasma Sources Sci. Technol.* **27** 125010
[37] Belenguer P and Boeuf J 1990 *Phys. Rev.* A **41** 4447
[38] Godyak V, Piejak R and Alexandrovich B 1992 *Plasma Sources Sci. Technol.* **1** 36
[39] Brinkmann R 2016 *Plasma Sources Sci. Technol.* **25** 014001
[40] Lieberman M, Lichtenberg A and Savas S 1991 *IEEE Trans. Plasma Sci.* **1** 189
[41] Okuno Y, Ohtsu Y and Fujita H 1994 *Appl. Phys. Lett.* **64** 1623
[42] Zhang Q-Z, Sun J-Y, Lu W-Q, Schulze J, Guo Y-Q and Wang Y-N 2021 *Phys. Rev.* E **104** 045209
[43] Patil S, Sharma S, Sengupta S, Sen A and Kaganovich I 2022 *Phys. Rev. Res.* **4** 013059
[44] Hutchinson D, Turner M, Doyle R and Hopkins M 1995 *IEEE Trans. Plasma Sci.* **23** 636
[45] Turner M, Hutchinson D, Doyle R and Hopkins M 1996 *Phys. Rev. Lett.* **76** 2069
[46] Krimke R and Urbassek H 1995 *IEEE Trans. Plasma Sci.* **23** 103
[47] Barnat E, Miller P and Paterson A 2008 *Plasma Sources Sci. Technol.* **17** 045005
[48] You S *et al* 2011 *Thin Solid Films* **519** 6981
[49] Zheng B, Wang K, Grotjohn T, Schuelke T and Fan Q 2019 *Plasma Sources Sci. Technol.* **28** 09LT03
[50] Oberberg M, Engel D, Berger B, Wölfel C, Eremin D, Lunze J, Brinkmann R, Awakowicz P and Schulze J 2019 *Plasma Sources Sci. Technol.* **28** 115021
[51] Joshi J, Binwal S, Karkari S and Kumar S 2018 *J. Appl. Phys.* **123** 113301
[52] Kushner M 1989 *J. Appl. Phys.* **65** 3825
[53] Krimke R, Urbassek H, Korzec D and Engemann J 1994 *J. Phys. D: Appl. Phys.* **27** 1653
[54] Wang L, Wen D-Q, Hartmann P, Donkó Z, Derzsi A, Wang X-F, Song Y-H, Wang Y-N and Schulze J 2020 *Plasma Sources Sci. Technol.* **29** 105004
[55] Zheng B, Fu Y, Wang K, Schuelke T and Fan Q 2021 *Plasma Sources Sci. Technol.* **30** 035019
[56] Eremin D *et al* 2023 Electron dynamics in planar radio frequency magnetron plasmas: II. Heating and energization mechanisms studied via a 2d3v particle-in-cell/Monte Carlo code *Plasma Sources Sci. Technol.* accepted (https://doi.org/10.1088/1361-6595/acc47f)
[57] Berger B, Eremin D, Oberberg M, Engel D, Wölfel C, Zhang Q-Z, Awakowicz P, Lunze J, Brinkmann R and Schulze J 2023 Electron dynamics in planar radio frequency magnetron plasmas: III. comparison of experimental investigations of power absorption dynamics to simulation results accepted (https://doi.org/10.1088/1361-6595/acc480)
[58] Panjan M 2019 *J. Appl. Phys.* **125** 203303
[59] Lucken R, Tavant A, Bourdon A, Lieberman M and Chabert P 2020 *Plasma Sources Sci. Technol.* **29** 065014
[60] Xu L, Eremin D and Brinkmann R P 2021 *Plasma Sources Sci. Technol.* **30** 075013
[61] Oberberg M, Kallähn J, Awakowicz P and Schulze J 2018 *Plasma Sources Sci. Technol.* **27** 105018
[62] Oberberg M, Berger B, Buschheue M, Engel D, Woelfel C, Eremin D, Lunze J, Brinkmann R, Awakowicz P and Schulze J 2020 *Plasma Sources Sci. Technol.* **29** 075013
[63] Trieschmann J, Shihab M, Szeremley D, Elgendy A, Gallian S, Eremin D, Brinkmann R and Mussenbrock T 2013 *J. Phys. D: Appl. Phys.* **46** 084016
[64] Qiu W 2001 Electron series resonance plasma discharges: unmagnetized and magnetized *PhD Thesis* University of California, Berkeley
[65] Wesson J 2011 *Tokamaks* 4th edn (Oxford: Oxford University Press)
[66] Eremin D 2022 *J. Comput. Phys.* **452** 110934
[67] Chen G, Chacón L and Barnes D 2011 *J. Comput. Phys.* **230** 7018
[68] Barnes D and Chacón L 2021 *Comput. Phys. Commun.* **258** 107560
[69] Vahedi V and Surendra M 1995 *Comput. Phys. Commun.* **87** 179
[70] Mertmann P, Eremin D, Mussenbrock T, Brinkmann R and Awakowicz P 2011 *Comput. Phys. Commun.* **182** 2161
[71] Phelps A and Petrović Z 1999 *Plasma Sources Sci. Technol.* **8** R21
[72] Phelps A 1994 *J. Appl. Phys.* **76** 747
[73] Markidis S and Lapenta G 2011 *J. Comput. Phys.* **230** 7037
[74] Turner M, Derzsi A, Donkó Z, Eremin D, Kelly S, Lafleur T and Mussenbrock T 2013 *Phys. Plasmas* **20** 013507
[75] Charoy T *et al* 2019 *Plasma Sources Sci. Technol.* **28** 105010
[76] Villafana W *et al* 2021 *Plasma Sources Sci. Technol.* **30** 075002
[77] Wilczek S, Schulze J, Brinkmann R P, Donkó Z, Trieschmann J and Mussenbrock T 2020 *J. Appl. Phys.* **127** 181101
[78] Surendra M and Dalvie M 1993 *Phys. Rev.* E **48** 3914
[79] Hazeltine R and Waelbroeck F 2004 *The Framework of Plasma Physics* (Boulder, CO: Westview Press)